Title
Novel Protein therapeutics delivery systems based on multifunctional nanostructures

Author
Lee, Kunwoo

Publication Date
2016

Peer reviewed|Thesis/dissertation

Novel Protein therapeutics delivery systems based on multifunctional nanostructures

by

Kunwoo Lee

A dissertation submitted in partial satisfaction of the

requirements for the degree of

Joint Doctor of Philosophy

with the University of California, San Francisco

in

Bioengineering

in the

Graduate Division

of the

University of California, Berkeley

Committee in charge:

Professor Niren Murthy, Chair

Professor David V. Schaffer

Professor Dirk Hockemeyer

Spring 2016

Novel Protein therapeutics delivery systems based on multifunctional nanostructures

By
Kunwoo Lee

Abstract

Novel Protein therapeutics delivery systems based on multifunctional nanostructures

by

Kunwoo Lee

Joint Doctor of Philosophy

with the University of California, San Francisco

in Bioengineering

University of California, Berkeley

Professor Niren Murthy, Chair

Delivery is a key challenge in novel protein therapeutic development. Even though numerous proteins are potential therapeutic candidates, a lack of delivery method limits the development of protein therapeutics. I have studied protein delivery and designed three novel delivery systems: gold nanoparticle based polymer particle system, multifunctional oligonucleotide, and nanostructured microparticles. Each of delivery system was designed to deliver CRISPR/Cas9 ribonucleoprotein, transcription factors, and oral protein drugs.

First of all, CRISPR/Cas9 is a great tool in genome editing field. Moreover, CRISPR/Cas9-mediated genome editing has the potential to revolutionize the treatment of genetic diseases and the development of cell-based therapies. However, precise gene editing with Cas9 is still challenging *in vivo* because it requires simultaneous and efficient delivery of Cas9, guide RNA, and donor DNA into cells. We designed a gold nanoparticle-based delivery vehicle, CRISPR-Gold, which can directly deliver Cas9 protein, guide RNA (gRNA), and donor DNA *in vitro* and *in vivo* and efficiently induce homology directed repair (HDR). CRISPR-Gold is composed of gold nanoparticles assembled with the Cas9-gRNA ribonucleoprotein (RNP) complex, donor DNA, and an endosomal disruptive polymer. We demonstrate that CRISPR-Gold can induce HDR in human stem cells and mouse primary cells with an efficiency that is significantly higher than conventional transfection methods. Notably, we show that CRISPR-Gold can correct a nonsense mutation in the dystrophin gene that causes Duchenne muscular dystrophy in *mdx* mice, and restore dystrophin protein expression in mouse muscle after a single injection.

Another potential protein therapeutic group is the transcription factor, which can have broad effects in gene regulation. We designed a novel multifunctional oligonucleotide, termed DARTs, which can deliver transcription factors with high efficiency *in vivo*. DARTs are composed of an oligonucleotide that contain a transcription factor binding sequence and hydrophobic membrane disruptive chains that are masked by acid cleavable galactose residues. DARTs have a unique molecular architecture, which allows them to bind transcription factors, trigger endocytosis in hepatocytes, and stimulate endosomal escape. The DARTs target hepatocytes as a result of the

galactose residues and can disrupt endosomes efficiently with minimal toxicity because the unmasking of their hydrophobic domains selectively occurs in the acidic environment of the endosome. DARTs showed efficient delivery of the transcription factor Nrf2 to the liver, catalyzed the transcription of Nrf2 downstream genes, and rescued mice from acetaminophen induced liver injury.

Another method of delivery that continues to be in the process of improvement is the oral drug delivery system for protein therapeutics. Oral drug delivery faces challenges including harsh acidic environment, rapid clearance of drug, and limited paracellular transport of therapeutic molecules. We studied a nanostructured microparticle system to overcome the challenges with an engineering approach. We showed that planar silica particles coated with silicon nanowires loaded proteins efficiently. The planar particles increased the transepithelial permeation of the protein drug as a result of a larger surface area in contact with the cell layer.

Dedication

This work is dedicated to my parents,
Hwasoo Lee and Jungyeol Kim,
whose unconditional love and belief in me
is the reason for my accomplishments.
And to my sister,
Sihyun Lee
who has supported me.
And to many of professors and friends.

Acknowledgments

This dissertation is a result of the help and support of many people. I would like to thank my family, mentors, friends, colleague for all of their encouragement, and support throughout this process.

I wish to thank the members of my dissertation committee for advice and support during the course of PhD. Dr. Niren Murthy provided excellent research guidance and allowed an environment that encouraged me to think creatively and challenge myself. I really believe that my PhD was worthy and I have learned a lot. Dr. David Schaffer has been a great mentor and a role model. His insight and advice were priceless. Dr. Dirk Hockemeyer provided interesting insights and encouraged me to understand biology better. Moreover, Dr. Tejal Desai has inspired me to study drug delivery field and helped me guide through PhD. Her comments always encouraged me to make a step forward. Dr. Kevin Healy gave precious advice which allowed me to study regenerative medicine and tissue engineering. Dr. Jennifer Doudna inspired me in many ways and allowed me to dream big. Her warm encouragement meant a lot to me. I was fortunate to have great scientists around who collaborated with me. I was not able to conduct CRISPR-Cas9 work without Dr. Irina Conboy and Dr. Mike Conboy. They have been amazing collaborators. There are a lot more collaborators: Dr. Jacob Corn, Dr. Kazunori Kataoka, Dr. Albert Pisano, Dr. Stanley Qi, Dr. Nicole King, Dr. Vuk Uskoković, Hyunjin Kim, Mark Dewitt, Wen-chin Huang, Dawn Spelke, Freeman Lan, Palmer Yu, Hongyun So, Jacques Deguine, Mary West, Hector Neira. I also appreciate Seung-Wuk Lee, Luke Lee, and Dorian Liepmann for great advice.

I would also like to thank the past and present members of Murthy Laboratory. All of their inputs helped this work. I was fortunate to work with great undergraduate students: Richard Tang, Nithya Ligampalli, Youngsoon Park, Anirudh Rao, and Kevin Chang and graduate students: George Lin, Zoey Huang, and Vanessa Mackley.

There are a number of close friends that have helped make my life exciting. I would like to mention some of my great friends by name: Hyeyoung Lee, Hyo Min Park, Hyunjin Kim, Hyunho Park, Gil Young Cho, Hyang-keun Yoo, Chanwoo Oh, Hyeshin Na, Taewoo Kim, Dongmin Sohn, Dongjin Seo, Kyunam Kim, Youngwook Kwon, Hyukjun Kwon, Seung Min Woo, Eugene Choo, Jaeyoung Choi, Seung-min Park, Kangwook Lee, Jyungmean Son, Ryan Joo, Ye-eun Kim, Sangmin Park, Bong-sik Choi, Minjae Do, Jinwoo Kim, Kuhong Jeong, Hoduk Cho

There are close scientists who have inspired me: Yumi Kim, Yongjin Choi, Sung-yon Kim, Kyuri Lee, Hyukjin Lee, Hak-sung Kim, Han Yong-Mahn, Sangyong Jon, Je-Kyun Park

Special thanks to my life scientist and tennis buddies: John Kim, Jiyung Shin, Soojung Yang

I would like to thank all members of BEAST who have helped my graduate student life memorable. Freeman Lan, Simon Lee, Harrison Liu, Daniel Liu, Elena Kassianidou, Anusuya Ramsubramanian, Tuan Tran, Weixi, Zhong, Wenwen Jiang, Yuchen Pan, Annie Ouyang,

Pamela Jreji, Jennifer Soto, Zach Russ, Malav Desai, Paul Keselman, Matt Bakalar, Wen-Chin Huang, Shang Song, Sze Yue Wong, Saurabh Belsare, Benjamin Epstein, Todd Duncombe, Tim Downing, Junren Sia, Kristin Olson, SarahJane Taylor.

Your friendships are so greatly appreciated and my days in graduate school will never be forgotten.

I would also like to thank all of the funding sources including NIH grants and the Siebel Scholars Foundation.

Table of Contents

Chapter 1: Introduction

1.1 Dissertation Introduction

In just the past few decades, an increasing number of protein therapeutics have been developed and they have the potential to improve the quality of human life. However, most protein therapeutics fall into a small category that act extracellularly, mainly growth factors, hormones, and antibodies. Even though numerous intracellular proteins have the potential to serve as novel therapeutics, most of them cannot be developed further due to the challenge of delivering proteins inside cellular membrane. For this reason, the delivery of macromolecules across the cellular membrane or epithelial tissue has been an area of great interest in bioengineering and medicine. This dissertation explores multifunctional nanostructures that can serve as novel protein delivery systems. Specifically, some proteins that hold potential in therapeutics include CRISPR/Cas9, transcription factors and orally administered protein therapeutics.

1.2. Dissertation outline

In **Chapter 2**, we explore a nanoparticle system for delivering CRISPR/Cas9 protein and guide RNA. This chapter describes how the nanoparticle system is synthesized and characterized. In addition, genome editing tests in various cell types will be discussed. The system was tested in a mouse model system that has a mutation is very similar to the one causing Duchenne muscular dystrophy in human.

In **Chapter 3**, we will explain how a transcription factor delivery vehicle, termed DART, delivers the transcription factor Nrf2. The synthesis of DARTs and characterization are discussed. For efficient delivery, we designed a multifunctional oligonucleotide structure with galactose, acetal linkage, and a transcription factor binding DNA sequence for targeting, endosomal escape, and transcription factor loading, respectively. *In vitro* and *in vivo* Nrf2 deliveries were investigated and therapeutic potential of Nrf2 transcription factor delivery will be discussed.

In **Chapter 4**, nanostructured biomaterials for protein delivery are discussed. Protein delivery through oral administration is challenging due to short retention time in the small intestine and low bioavailability. We designed planar microparticles with nanowires to increase drug loading, retention time, and delivery efficiency. Unique nanostructured biomaterials have shown interesting properties in the drug delivery field and our study investigates shape effect of particles and the effects of nanostructure in paracellular delivery path.

Chapter 2: Genome editing in vivo with the delivery of Cas9 ribonucleoprotein and donor DNA complexed to gold nanoparticles

2.1 Introduction

CRISPRs(clustered regularly interspaced palindromic repeats) are a series of short repeated sequence in the genome of numerous bacteria and archaea[1]. The discovery of S. pyogenes CRISPR-Cas9 system and application of it as a dual-RNA-guided DNA endonuclease has revolutionized the way genome editing is conducted nowadays[2–4]. Specific genome editing using CRISPR-Cas9 has proved its potential usage in human cells[4–8].

Genome editing with Cas9-based therapeutics have the potential to treat a variety of incurable genetic diseases[9,10]. However, viral delivery is currently the only effective method for genome editing both *in vitro* and *in vivo*[10–12,5], and is challenging to translate because of the toxicity generated from viral vectors and the genomic damage caused by the sustained expression of Cas9[5,7]. In contrast to gene therapy, genome editing through directly delivering Cas9 RNP and donor DNA holds great clinical potential, because it avoids the toxicity problems of viral vectors, and minimizes off-target genomic damage by using Cas9 protein[5,7,8]. In addition, translating therapeutics based on the Cas9 protein will be significantly easier than gene therapy based methods, because protein therapeutics are widely used in medicine and established methods for their large-scale production, analysis, and toxicity assessment have been developed. Despite its promise, developing Cas9-based therapeutics remains challenging due to the lack of methods available to deliver Cas9 protein, guide RNA(gRNA), and donor DNA simultaneously into cells.

Among various genetic diseases that can be cured by CRISPR/Cas9 therapy, Duchenne muscular dystrophy(DMD) is a genetic disease with large unmet medical need, which affects 1/3500 boys and causes mortality by the early 20s[13]. DMD is caused by mutations in the dystrophin gene, which prevent the expression of the dystrophin protein[10,14,15]. The dystrophin protein is critical for maintaining healthy muscle fibers, and patients with DMD lose their muscle tissue and eventually die from the inability to breath due to wasting of the diaphragm and the intercostal muscle[13]. This study focused on developing a new delivery vehicle to delivery Cas9 protein, gRNA, and donor DNA to repair a mutation causing DMD.

2.2 Materials and Methods

2.2.1 Materials

Oligonucleotides were purchased from Integrated DNA Technologies (IDT, Coralville, IA). Gold nanoparticles (15 nm) were purchased from BBI solutions. Sodium citrate and 4-(2-hydroxyethyl) piperazine-1-ethanesulfonate (HEPES) were purchased from Mandel Scientific (Guelph, ON). Sodium silicate was purchased from Sigma Aldrich (St. Louis, MO). Phusion High-fidelity DNA Polymerase was purchased from NEB (Ipswich, MA). The Megascript T7 kit, the Megaclear kit, PageBlue solution, and the PureLink genomic DNA kit were purchased from Thermo Fischer (Waltham, MA). Mini-PROTEAN TGX Gels (4-20%) were purchased from Bio-Rad (Hercules, CA). MTeSR-1 media gentle cell dissociation reagent was purchased

from StemCell Technologies (Vancouver, Canada). Matrigel was purchased from BD Biosciences (San Jose, CA). DMEM media, non-essential amino acids, penicillin-streptomycin, DPBS and 0.05% trypsin were purchased from Life Technologies (Carlsbad, CA). Oct-4 antibody (sc-5279) and SSEA-4 antibody were purchased from Santa Cruz (Santa Cruz, CA). Sox2 antibody (AB5603), TRA-1-60 antibody (MAB4360), and EMD Millipore Amicon Ultra-4 100kDa were purchased from Millipore (Germany).

2.2.2 Expression and purification of Cas9

The full-length catalytically active *Streptococcus pyogenes* Cas9 was cloned into a custom pET-based expression vector encoding an N-terminal 6xHis-tag followed by maltose-binding protein (MBP) and a TEV protease cleavage site, as well as two SV40 nuclear localization signal (NLS) peptides at its C-terminus. Recombinant Cas9 protein was expressed in *Escherichia coli* strain BL21 (DE3) (Novagen. Highly purified Cas9 protein was stored in 50 mM HEPES pH 7.5, 300 mM NaCl, 10% glycerol, 100 μM TCEP at -80℃. *S. pyogenes* Cas9 D10A nickase was expressed and purified following the same procedure. Cas9 protein concentration was determined by a NanoDrop spectrophotometer from the absorbance at 280 nm.

2.2.3 In Vitro T7 Transcription of sgRNA

Oligonucleotide primers for sgRNA production were purchased from IDT, with the forward primer containing a T7 promoter sequence. The DNA template for *in vitro* sgRNA transcription was prepared by overlapping PCR. Briefly, the T7 forward template (20 nM), T7Rev-Long template (20 nM), T7 forward primer (1 μM), and T7 reverse primer (1 μM), were mixed with PCR with Phusion Polymerase (NEB) for PCR amplification according to the manufacturer's protocol. RNA *in vitro* transcription was performed with the MEGAscript T7 kit (Thermo Fisher) and purification of the resulting RNA was conducted using the MEGAclear kit, following the manufacturer's protocol. The transcribed sgRNA was eluted into 50 mM HEPES pH 7.5, 300 mM NaCl, 10% (vol/vol) glycerol, and 100 μM TCEP. The concentration of sgRNA was determined with a Nanodrop 2000 and the final sgRNA products were stored at -80 ℃ for subsequent experiments.

2.2.4 Synthesis of CRISPR-Gold

A representative synthesis of CRISPR-Gold is described in this section. Gold nanoparticles (GNP) (15 nm in diameter, 450 nM) were reacted with a 5' thiol modified single stranded oligonucleotide (DNA-SH), 25 bases in length (200 μM), which had a region complementary to the donor DNA sequence, the reaction was performed in an Eppendorf tube in 20 mM HEPES buffer, in a 100 μL volume. The NaCl concentration of the reaction was slowly increased to 400 mM and the reaction was allowed to proceed overnight. Unconjugated DNA-SH was removed by centrifugation at 17,000 g for 15 min, and washing two times with 20 mM HEPES buffer. The resulting Gold-DNA conjugated was hybridized with the donor oligonucleotide. The donor DNA (100 μM concentration, 10 μL) was added to the GNP-DNA solution in 20mM HEPES with 50mM NaCl (100 μL), and incubated at 65 ℃ for 10 min, and gradually brought to room temperature (-2 ℃/min). The GNP-Donor solution was stored at 4 ℃ until further use. CRISPR-Gold was synthesized by a layer-by-layer method, right before the *in vitro* and *in vivo* experiments. Cas9 (8 μg in 10 μL) and gRNA (2 μg in 10 μL) were mixed in 80 μL of Cas9 buffer (50 mM Hepes (pH 7.5), 300 mM NaCl, 10% (vol/vol) glycerol, and 100 μM TCEP) for 5

min at RT, and this solution was then added to the GNP-DNA-Donor solution (0.45 pmole of GNP). Freshly diluted sodium silicate (60 mM, 2 μL) was added to the GNP-DNA-Donor-Cas9 RNP solution and incubated for 5 min at RT. The mixture was centrifuged using an EMD Millipore Amicon Ultra-4 100 kDa at 3,000 rpm for 5 min to remove unbound sodium silicate. The recovered GNP-DNA-Donor-Cas9 RNP-silicate were resuspended in 20mM HEPES buffer (100 μL) and PAsp(DET) was added to generate a final concentration of 30 μg/mL and incubated for 15 min at RT to form the last layer of CRISPR-Gold. The synthetic procedure described above is scalable and can be used to prepare more concentrated CRISPR-Gold solutions.

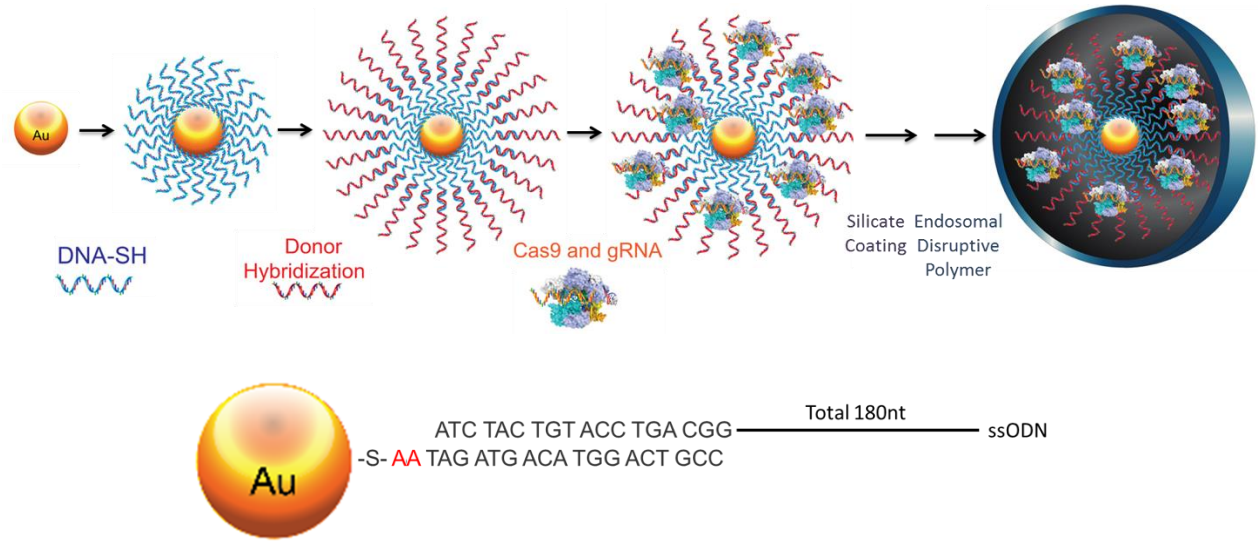

Figure 2.1. Synthesis of CRISPR-Gold. Gold nanoparticles 15 nm in diameter were conjugated with a 5′ thiol modified single stranded DNA (DNA-SH), and hybridized with single stranded donor DNA. A CXCR4 donor DNA sequence is presented as an example. The DNA-SH sequence is complementary to 18 nucleotides in the 3′ end of the donor DNA. This CRISPR-Gold intermediate is sequentially complexed with Cas9 ribonucleoprotein (RNP), sodium silicate, and PAsp(DET) to obtain CRISPR-Gold.

2.2.5 Absorbance spectra and zeta potential analysis of CRISPR-Gold

The synthetic intermediates in the synthesis of CRISPR-Gold, GNPs, GNP-DNA, GNP-DNA-donor DNA, GNP-Cas9 RNP and GNP-Cas9 RNP-PAsp(DET) were characterized by UV-vis spectroscopy. The absorbance spectra of each sample were measured with a UV-vis spectrophotometer (NanoDrop 2000, Thermo scientific). Zeta potential measurements were also made on each intermediate at 25 ℃. Zeta potential measurements were made with a Zetasizer Nano ZS instrument (Malvern Instruments Ltd., Worcestershire, UK), and electrophoretic mobility was measured in a folded capillary cell (DTS 1060, Malvern Instruments), the zeta potential was calculated using the Smoluchowski equation.

2.2.6 Cell culture

2.2.6.1 BFP expressing HEK cell culture

BFP-HEK cells were generated by infection of HEK293T cells with a BFP-containing lentivirus, followed by FACS-based enrichment, and clonal selection for cells expressing BFP with no silencing after 2-4 weeks. Virus was generated by transfection of HEK293FT cells with a custom lentiviral vector containing a BFP gene driven by the pEF1 promotor, cloned into a Lenti X1 DEST Blast backbone by Gateway cloning (Life Technologies, Inc.). Reporter cell lines were generated by infection of HEK293T cells with lentivirus, at low MOI (as estimated by FACS 3 days post-infection). BFP-positive cells were enriched by FACS, grown out, and sorted into clones by FACS. A clone with high constitutive BFP fluorescence (>99% BFP-positive) was selected and cultured. To edit BFP-HEK to GFP, cells were plated at a density of 5×10^4 cells per well in a 24 well plate, a day before CRISPR-Gold experiments, and cultured in DMEM with 10% FBS, 1× MEM non-essential amino acids, and 100 μg/mL Pen Strep.

2.2.6.2 Stem cell culture

Human H9 embryonic stem (hES) cells and human induced pluripotent stem (hiPS) cells were maintained in Matrigel-coated 6-well tissue culture plates. Cell culture plates were coated with Matrigel diluted to 12.5 μL/mL in DMEM and incubated for an hour at 37 ℃[1]. MTeSR-1 medium (StemCell Technologies) was added to the cells every day and the cells were passaged every 4-6 days. Gentle cell dissociation reagent (StemCell Technologies) was used for cell detachment, according to the manufacturer's protocol. Stem cells were passaged into 24 well plates, at a density of 2×10^4 cells per well, 3 days prior to Cas9 transfection.

2.2.6.3 Mouse primary bone marrow derived dendritic cell culture

Bone marrow cells were obtained from the tibias and femurs of mice. Bone marrow cells were plated in complete medium containing granulocyte-macrophage colony-stimulating factor (GM-CSF) (10 ng/mL; Peprotech) for 6 days to allow for differentiation into DCs. Cas9 transfection was conducted on Day 6.

2.2.7 Cell transfection

For all of the gene editing experiments with CRISPR-Gold, electroporation, or lipofectamine, transfections were conducted on cells when they reached a density of 10^5 cells per well (in 24 well plates). The sample sizes ranged between n = 3 to n = 6. This sample size was chosen based on previous papers on Cas9 protein delivery, which demonstrated that n = 3 to n = 6 was sufficient to generate statistically significant data[2].

2.2.8 CRISPR-Gold treatment

CRISPR-Gold particles were formed as described in S4. For all of the in vitro cell experiments, 10^5 cells in 0.5 mL were treated with 0.45 pmole GNP-Donor, Cas9 (8 μg), gRNA (2 μg), 2 μL sodium silicate (60 mM), and 3 μg PAsp(DET). The details of the CRISPR-Gold synthesis are described in section S5. Cas9 and gRNA solution were mixed in Cas9 buffer (50 mM Hepes (pH 7.5), 300 mM NaCl, 10% (vol/vol) glycerol, and 100 μM TCEP) for 5 min at RT and added to the GNP-Donor solution. Freshly diluted sodium silicate (60 mM, 2 μL) was added to the GNP solution and incubated for 5 min at RT. The reaction mixture was centrifuged using an EMD Millipore Amicon Ultra-4 100 kDa at 3,000 rpm for 5 min to remove unbound sodium silicate. The recovered gold nanoparticles were resuspended in 20mM HEPES buffer (100 μL) and PAsp(DET) polymer was added to a final concentration of 30 μg/mL and incubated for 15 min at RT to form the last layer of CRISPR-Gold. CRISPR-Gold was added to the cells, in fresh serum

containing media, and incubated for 16 hr and then the medium was changed. The cells were incubated for a total of 3 days before genomic DNA extraction and analysis.

2.2.9 Nucleofection

Cells were detached by 0.05% trypsin or gentle dissociation reagent and spun down at 600 g for 3 min, and washed with PBS. Nucleofection was conducted using an Amaxa 96-well Shuttle system following the manufacturer's protocol, using 10 μL of Cas9 RNP and DNA donor (Cas9 : 100 pmole, gRNA : 120 pmole, DNA donor : 100 pmole). After the nucleofection, 500 μL of growth media was added and the cells were incubated at 37 ℃ in tissue culture plates. The cell culture media were changed 16 hr after the nucleofection, and the cells were incubated for a total of 3 days before genomic DNA extraction and analysis.

2.2.10 Lipofection

Lipofectamine transfection with Cas9 was performed following the protocol described in Zuris et al. using 4.4 μg of Cas9, 1.2 μg of gRNA, and 1.2 μL of Lipofectamine 2000 in 100 μL total volume[2]. Additionally, donor DNA (250 ng) was mixed with lipofectamine (500 nL) and added to the transfection media, which contained the Cas9 RNP lipofectamine solution. The lipofection was conducted in OptiMEM media without serum, and an equal volume of 2x growth media was added to the cells after 1hr of lipofection to minimize cytotoxicity. The medium was changed 16 hr after the lipofection and the cells were incubated for a total of 3 days before genomic DNA extraction and analysis.

2.2.11 Cellular uptake of CRISPR-Gold

The uptake of CRISPR-Gold in primary immune cells and bone marrow derived dendritic cells, obtained from the bone marrow of C57BL/6J mice, was determined. Bone marrow derived dendritic cells were cultured on Matrigel coated plates for imaging. CRISPR-Gold (0.45 pmole gold nanoparticle) was incubated with 10^5 cells in culture media (500 μL) for 16 hr, the media was changed. After washing 3 times, the cells were observed with a Zeiss inverted microscope and images were taken using Zen 2015 software. Additionally, the treated cells were detached and centrifuged at 600 g for 2 min in Eppendorf tubes, and imaged with a digital camera to determine changes in cell color.

2.2.12 Flow cytometry analysis & Fluorescence microscopy

Flow cytometry was used to quantify the expression levels of BFP and GFP in BFP-HEK cells treated with CRISPR-Gold. The BFP-HEK cells were analyzed 7 days after Cas9 treatment. The cells were washed with PBS and detached by 0.05% trypsin. BFP expression was quantified using BD LSR Fortessa X-20 and GFP expression was quantified using Guava easyCyte™. Fluorescence images were taken with a fluorescence Zeiss inverted microscope using Zen 2015 software.

2.2.13 Sanger sequencing of the BFP/GFP gene

The GFP+ population was sorted from BFP-HEK cells that had been treated with CRISPR-Gold (7 days after treatment). Cells were detached by 0.05% trypsin treatment and the GFP+ edited cells were sorted using a BD influx cell sorter (BD Biosciences) in the Berkeley flow cytometry facility. Genomic DNA was extracted from the GFP+ sorted cells and PCR amplification of the

BFP/GFP gene was conducted. Sanger sequencing was conducted by Quintara Inc (CA, USA) and the sequence was analyzed with apE software.

2.2.14 PCR amplification of genomic DNA from transfected cells

Genomic DNA of 2×10^4 to 2×10^5 cells was extracted 3 days after transfection using the Purelink genomic DNA kit (Thermo Fisher). The concentration of genomic DNA was measured with a Nanodrop spectrophotometer. The target genomic DNA sequences (BFP, CXCR, and dystrophin) were amplified using primer sets and Phusion polymerase with high GC buffer according to the manufacturer's protocol. All primer sets were designed to anneal outside of the homology arms of the donor DNA in order to avoid amplifying the donor DNA. The PCR products were analyzed on a 1.5% (wt/vol) agarose gel casted with SYBR Safe (Thermo fischer).

2.2.15 Analysis of genome editing efficiency with restriction enzyme digestion and T7 Endonuclease I assay

The HDR efficiency in cells was determined with restriction enzyme digestion of PCR amplified target genes. Donor DNAs were designed to insert restriction enzyme sites, cleavable by either HindIII or DraI, into the target gene locus. The PCR amplicon of the CXCR4 locus and the PCR amplicon of the DMD locus were incubated with 10 units of HindIII and DraI, respectively. After 2 hr to 16 hr of incubation at 37C, the products were analyzed by gel electrophoresis using a 4-20% Mini-PROTEAN TGX Gel (Bio-rad) and stained with SYBR green (Thermo fischer). Individual band intensity was quantified using ImageJ and the HDR efficiency was calculated using the following equation: $(b + c) / (a + b + c) \times 100$ (a = uncleaved PCR amplicon, b and c = the cleavage products). The T7 endonuclease I assay was conducted to estimate the total DNA editing by cutting mismatched heteroduplex DNA from mutant DNA and wild-type DNA hybrid. Hybridization and T7E1 incubation were performed as described in Schumann et al.[8].

2.2.16 Cell viability assay

The relative cell viabilities of cells transfected with CRISPR-Gold, nucleofection, and lipofection were determined with a cell counting kit (Dojindo) using regular culture media supplemented with 10% (v/v) CCK solution. The CCK assay was conducted 2 days after the transfection.

2.2.17 Sanger sequencing of hES edited with CRISPR-Gold

The CXCR4 PCR amplicon of CRISPR-Gold treated hES cells were cloned into plasmids using a Zero Blunt TOPO PCR cloning kit (Life Technologies), following the manufacturer's instruction. Briefly, TOP10 *E.coli* were transformed with plasmids containing the PCR amplicons and cultured on LB plates containing kanamycin. Sanger sequencing of the CXCR4 gene cloned into the *E.coli* colonies was conducted by Quintara Bioscience (CA, USA).

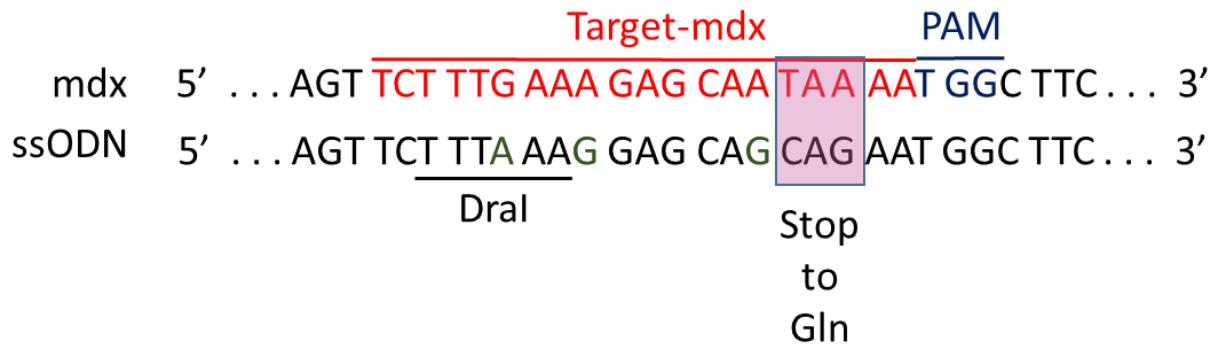

Figure 2.2. Sequence of genomic DNA targeted in the mdx mouse and the sequence of the donor DNA. The donor DNA is designed to replace the stop codon in the mutated dystrophin gene. Non-sense mutation and donor DNA sequence designed to repair the mutation are marked in the pink box, nucleotides marked in green (A, G, G) are silent mutations that prevent Cas9 activity on the edited sequence. Repair with the donor DNA sequence generates a DraI restriction enzyme site (TTTAAA), which is used for HDR analysis.

2.2.18 *In vivo* delivery of CRISPR-Gold in mdx mouse

Male C57BL/10ScSn mice and C57BL/10ScSn-*Dmdmdx*/J mice that contain a nonsense mutation in exon 23 of the dystrophin gene were purchased from Jackson Laboratory. The experiments were performed in a non-blinded manner, and the animals were not randomized. An n = 3 was selected because this sample size generally gives statistically significant results in this animal model. All animal studies were performed following authorized protocols and animals were treated in accordance with the policies of the animal ethics committee of the University of California at Berkeley. Three groups of mdx mice were used for this experiment. The experimental groups are: Control (no GNP) = mice injected with Cas9 RNP and donor DNA without gold nanoparticle (n=3), Control (no gRNA) = mice injected with CRISPR-Gold without gRNA (n=1), CRISPR-Gold = mice injected with CRISPR-Gold, which received CRISPR-Gold with all materials (n=3).

The injection was conducted in 2 month old mdx mice in the tibialis anterior(TA) muscle (10 μL per muscle) and gastrocnemius muscles (10 μL per muscle), using a Hamilton syringe. Two weeks after the injection, the muscles were harvested and analyzed. For all in vivo experiments, 6.75 pmole GNP, 120 μg Cas9, 30 μg gRNA, 30 μL sodium silicate (60mM), and 45 μg PAsp(DET) were injected per mouse. CRISPR-Gold particles were concentrated to a 60 μL total volume, which was distributed between the two hind legs, each hind leg received a total of 30 μL in 6 injection sites. Controls were injected with the same protocol. The experiments were conducted non-blinded and non-randomized way.

2.2.19 Deep sequencing analysis of CRISPR-Gold delivered muscle tissue

The genomic region of the Cas9 target sequence was amplified by PCR using Phusion high-fidelity polymerase according to the manufacturer's protocol. The amplicons were purified using ChargeSwitch PCR clean-up kit (Thermo Fischer). The Nextflex rapid illumine DNA-seq library prep kit was used to attach illumine adapters and PCR amplify the product for five cycles. PCR clean-up was performed one additional time. The Berkeley Sequencing facility performed

DNA quantification using a Qubit 2.0 Fluorometer (Life Technologies, Carlsbad, CA). BioAnalyzer for size analysis and qPCR quantification followed. The library was sequenced with the Illumina **HiSeq2500 in the Vincent Coates Genomic Sequencing Laboratory at UC Berkeley.**

2.2.20 Immunohistochemistry

Collected quadriceps and gastrocnemius muscles were frozen sectioned and fixed with 4% paraformaldehyde for 15 min at RT. After blocking for 1hr, a primary antibody against dystrophin (sc-47760) was incubated with the samples overnight. After extensive washing with PBS, a secondary antibody (sc-2005) was incubated with the samples for 1 hr at RT. The samples were stained with DAPI staining and analyzed via microscopy.

2.2.21 High throughput imaging of a whole muscle section

Glass slides with whole muscle sections stained for dystrophin protein were imaged with Molecular Devices ImageXpress Micro. On average, about 288 images were taken per slide with a 10 x objective lens. The images were analyzed using MetaXpress software to merge the images and create a montage of the whole muscle sections.

2.3 Results and Discussion

2.3.1 CRISPR-Gold Synthesis

CRISPR-Gold is designed to simultaneously deliver Cas9 protein, gRNA, and donor DNA *in vivo* to efficiently induce HDR. CRISPR-Gold is composed of gold nanoparticles 15 nm in diameter, which are complexed with donor DNA, Cas9 RNP and the endosomal disruptive polymer PASp(DET) (Fig. 2.3). The synthesis of CRISPR-Gold is based on a layer-by-layer approach and gold nanoparticle assembles donor DNA, Cas9 RNP, and endosomal disruptive polymers together into a single nanoparticle (Table 2.1 and Fig. 2.4 for characterization). CRISPR-Gold is designed to be internalized by cells via endocytosis due to the cationic PASp(DET) and the affinity of gold for cell membranes. After endocytosis, the PASp(DET) polymer on CRISPR-Gold triggers endosomal disruption, and causes the release CRISPR-Gold into the cytoplasm. Glutathione in the cytoplasm then causes the release of Cas9 RNP and donor DNA from CRISPR-Gold, via thiol exchange with the gold[16,17].

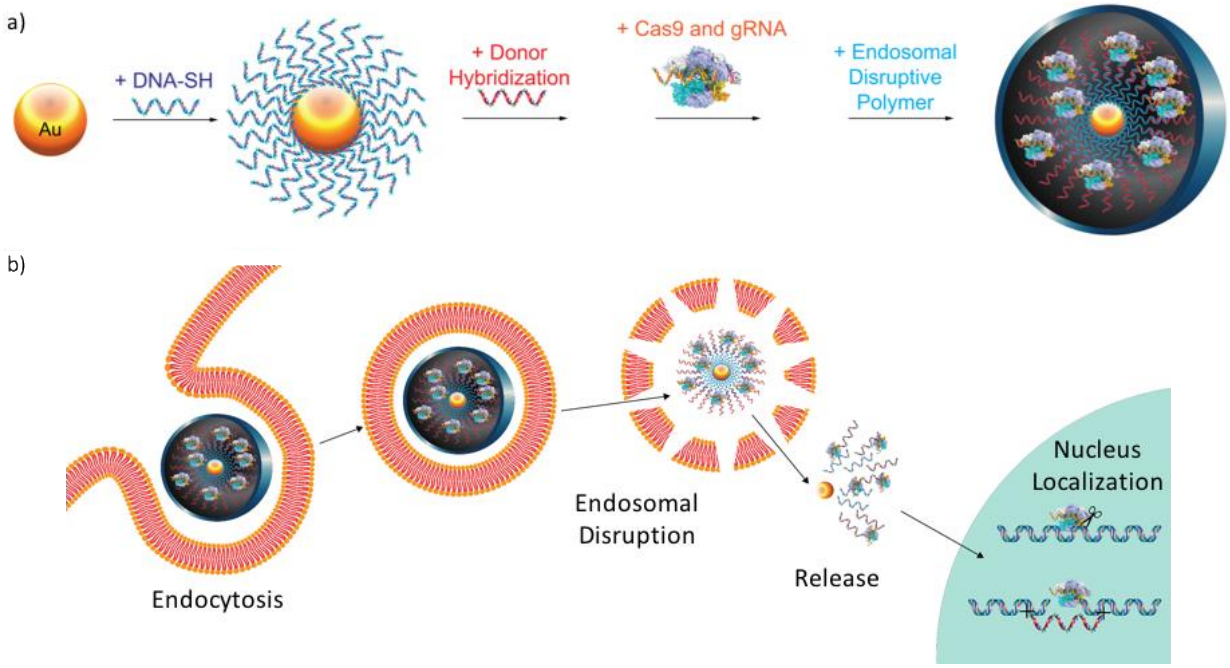

Figure 2.3. CRISPR-Gold can deliver Cas9 ribonucleoprotein and donor DNA *in vivo* and induce homologous directed repair with high efficiency.
a) CRISPR-Gold is composed of 15 nm gold nanoparticles conjugated to thiol modified oligonucleotides, which are hybridized with donor ssODN and subsequently complexed with Cas9 RNP, as well as the endosomal disruptive polymer PASp(DET).
b) CRISPR-Gold is internalized by cells *in vitro* and *in vivo* via endocytosis, triggers endosomal disruption, and releases Cas9 RNP and donor DNA into the cytoplasm. Nuclear delivery results in genome editing.

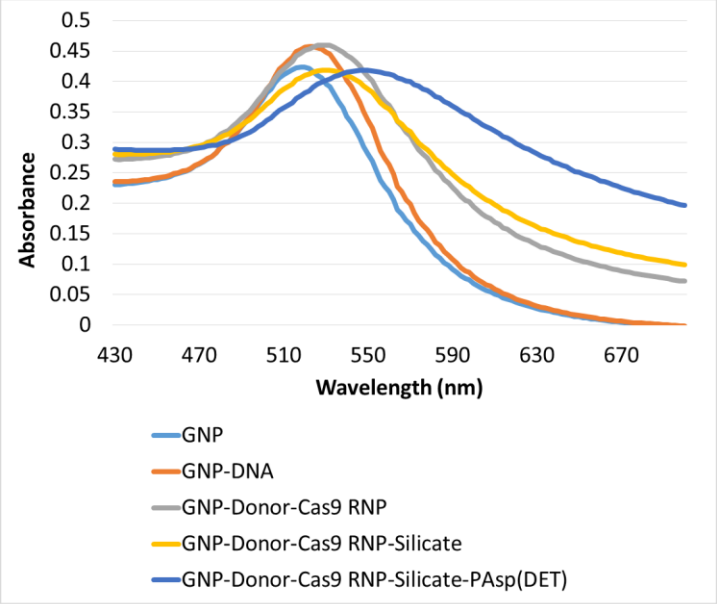

Particle	Peak (nm)
GNP	518
GNP-DNA	522
GNP-Donor-Cas9 RNP	528
GNP-Donor-Cas9 RNP-Silicate	532
GNP-Donor-Cas9 RNP-Silicate-PAsp(DET)	546

Figure 2.4. UV-vis absorbance of CRISPR-Gold synthetic intermediates. The absorption maxima of CRISPR-Gold intermediates are red shifted as CRISPR-Gold is sequentially constructed. Unmodified GNPs had an absorbance peak at 518 nm and the peak shifts to 522 nm for GNP-DNA, 528 nm for GNP-DNA-Cas9 RNP, and 546 nm for CRISPR-Gold.

Samples	Zeta Potential (mV) ± S.D.
GNP	-28.0 ± 14.2
GNP-DNA	-24.1 ± 16.4
GNP-Donor	-31.2 ± 15.8
GNP-Donor-Cas9	0.8 ± 8.0
GNP-Donor-Cas9 RNP	-13.2 ± 6.4
GNP-Donor-Cas9 RNP-Silicate	-18.9 ± 5.2
GNP-Donor-Cas9 RNP-Silicate-PAsp(DET)	18.0 ± 3.5

Table 2.1. Zeta potential analysis of CRISPR-Gold and its synthetic intermediates. Zeta potential measurements were performed on CRISPR-Gold and all of the synthetic intermediates generated during the construction of CRISPR-Gold. Zeta potential changes demonstrate the sequential synthesis of CRISPR-Gold. For example, GNP-Donor-Cas9 RNP-Silicate had a zeta potential of -18.9 mV and its surface charge density changes to +18.0 mV after the addition of the cationic polymer PAsp(DET).

2.3.2 CRISPR-Gold Test in BFP-HEK cells

We first performed experiments on BFP expressing HEK293 (BFP-HEK) cells to determine if CRISPR-Gold could deliver Cas9 RNP and donor DNA simultaneously to cells and efficiently induce HDR. CRISPR-Gold was hybridized with a single-stranded donor oligonucleotide (ssODN) homologous to the BFP gene, which contained a two base-pair substitution that converts the BFP gene into the GFP gene. CRISPR-Gold was then incubated with BFP-HEK cells and the HDR efficiency was determined by measuring the conversion of BFP to GFP *via* flow cytometry. Figure 2.5 demonstrates that CRISPR-Gold can efficiently induce HDR in BFP-HEK cells, which induced 18.3% of the BFP-HEK cells to express GFP.

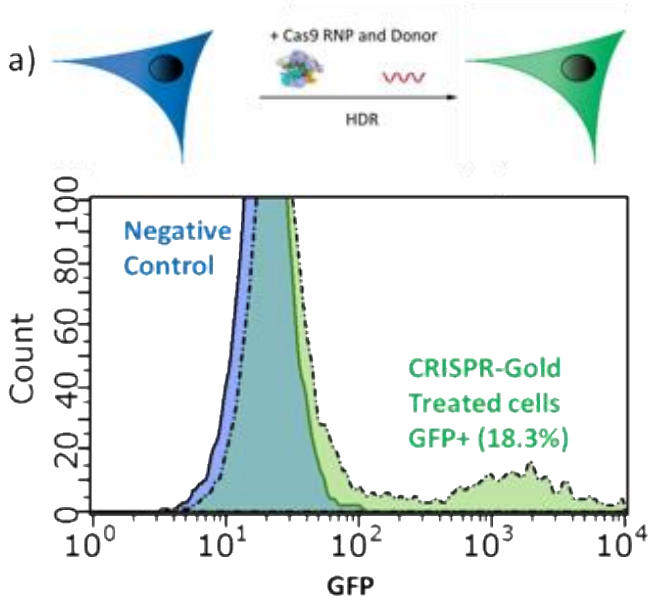

Figure 2.5. CRISPR-Gold can edit the genome of BFP-HEK cells efficiently.
CRISPR-Gold can induce HDR in BFP-HEK cells by delivering Cas9 RNP and a donor DNA. 18.3% of BFP-HEK cells were converted to GFP expressing cells, after treatment with CRISPR-Gold. GFP expression due to BFP sequence editing was determined by flow cytometry.

Sanger sequencing was performed on the GFP expressing cells collected with fluorescence-activated cell sorting (FACS). The sequence of the edited cells matched the donor DNA sequence of CRISPR-Gold, further confirming HDR (Fig. 2.6).

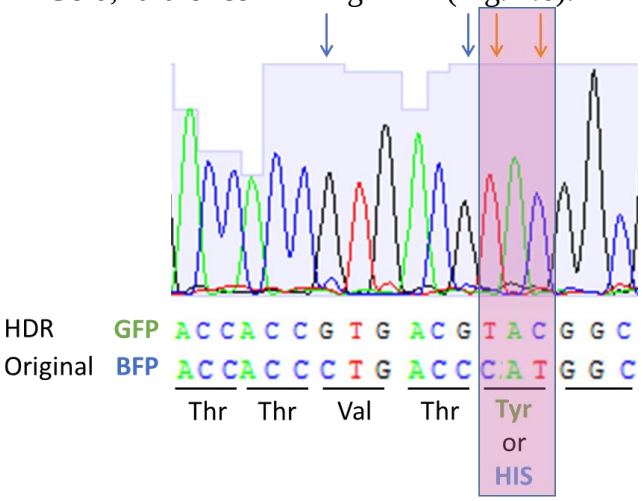

Figure 2.6. Sanger sequencing of CRISPR-Gold induced GFP positive cells confirms that HDR occurred in these cells. The BFP gene of cells treated with CRISPR-Gold or untreated cells was amplified by PCR, sequenced, and analyzed for HDR. GFP expressing cells had a 4-nucleotide edit that matches the donor DNA sequence. Orange arrows in the pink box indicate the corrected allele and green arrows indicate the silent mutation sites inserted to prevent Cas9 activity on the edited sequence.

2.3.3 CRISPR-Gold test in primary and stem cells

CRISPR-Gold has the potential to induce HDR in a wide variety of cell types because of its low toxicity and the universal uptake of gold nanoparticles by cells (Fig. 2.7).

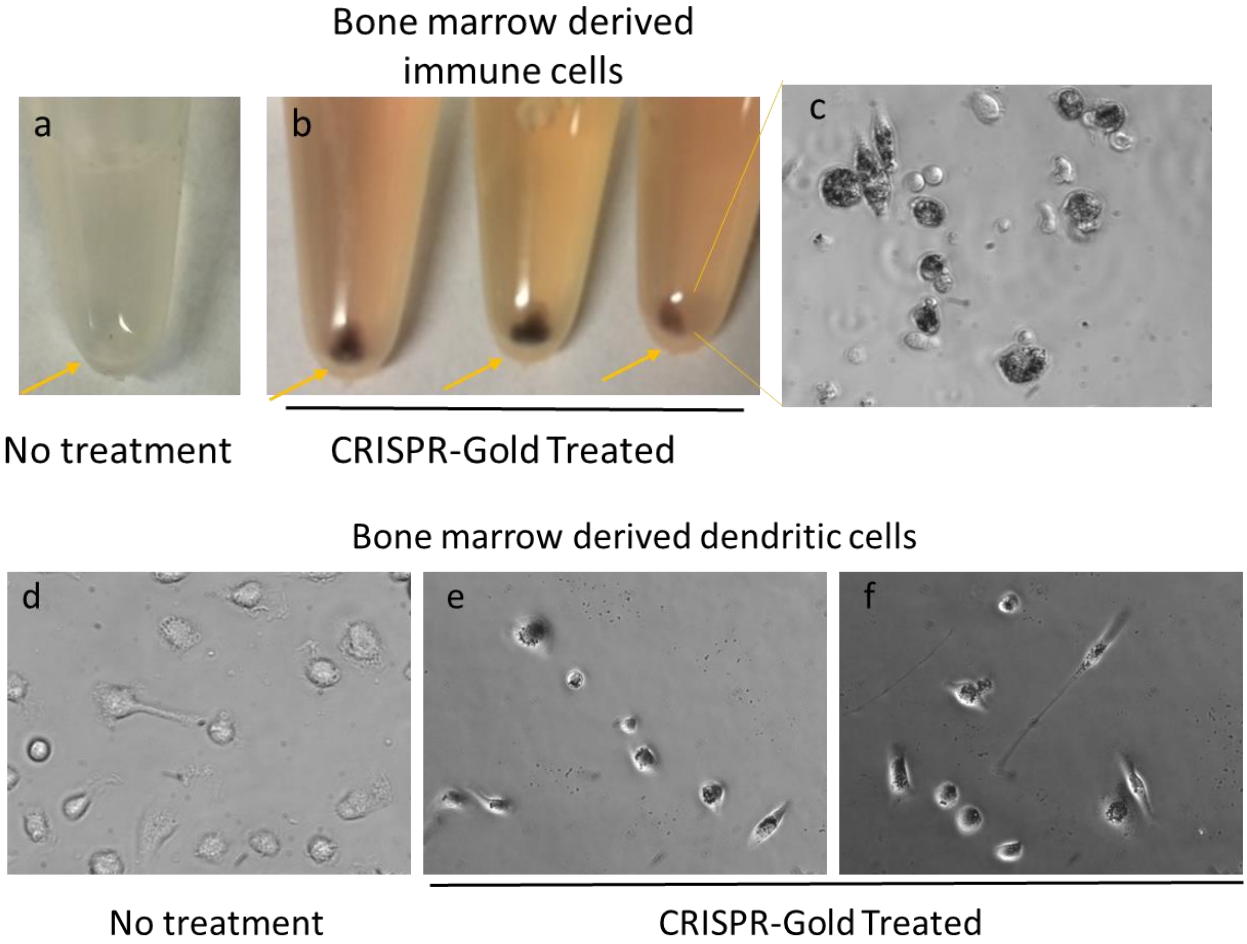

Figure 2.7. Bone marrow derived primary immune cells internalize CRISPR-Gold. a) Control cells without CRISPR-Gold treatment are transparent. b) Cells treated with CRISPR-Gold are dark brown indicating the presence of gold nanoparticles, yellow arrows indicate cell pellets. c) A bright field microscopic image shows that bone marrow derived immune cells have gold nanoparticle aggregates inside cells. d, e, f) Bright field microscopic images of bone marrow derived dendritic cells, with and without CRIPSR-Gold treatment. Dark spots indicate the presence of gold nanoparticles. Width of microscopic images is 100 μm.

Primary cells and stem cells are the cornerstone of a wide variety of cell-based technologies including cell and tissue transplants and the generation of transgenic mice. However, genome editing *via* HDR in primary cells and stem cells still remains a major challenge[7,18]. Therefore, we performed experiments to determine if CRISPR-Gold could induce HDR in human stem cells and primary cell cultures. We selected the CXCR4 gene as a target for HDR in human cells because of the widespread interest in editing this gene for HIV therapy[7,8,19]. In order to study HDR-induced insertion into the CXCR4 gene, human embryonic stem (hES) cells and human induced pluripotent stem (hiPS) cells were incubated with CRISPR-Gold composed of a guide RNA that targets CXCR4 gene and a donor DNA bearing a restriction site. The HDR efficiency of CRISPR-Gold was determined *via* restriction enzyme digestion and

further confirmed by Sanger sequencing. Figure 2.8 demonstrates that CRISPR-Gold can induce HDR in hES and hiPS cells with significantly higher efficiency than either lipofectamine or nucleofection. In addition, CRISPR-Gold has a significant advantage over nucleofection due to its low toxicity and minimal perturbation on cell phenotype (Fig. 2.9).

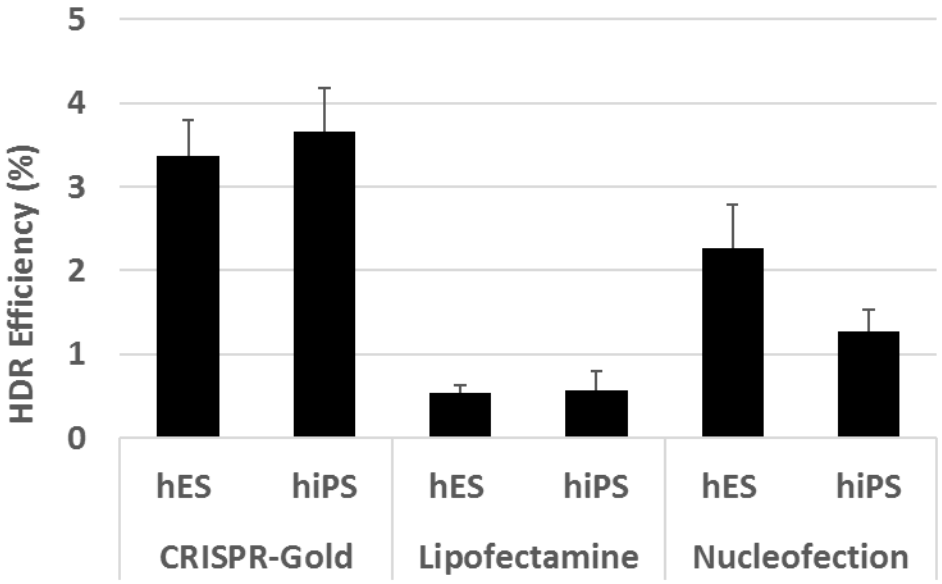

Figure 2.8. CRISPR-Gold induces HDR in hES and hiPS cells with higher efficiency than lipofectamine or nucleofection. Cells were treated with CRISPR-Gold that contained a donor sequence with a HindIII cleavage site, and a guide RNA that targeted the CXCR4 gene. The CXCR4 gene was amplified by PCR and the HDR efficiency was determined by quantifying HindIII cleavage of the CXCR4 PCR amplicon. Mean ± S.E, n=3. One-way ANOVA test had a p= 0.0066 for hES samples and p=0.0023 for hiPS samples, and are statistically significant.

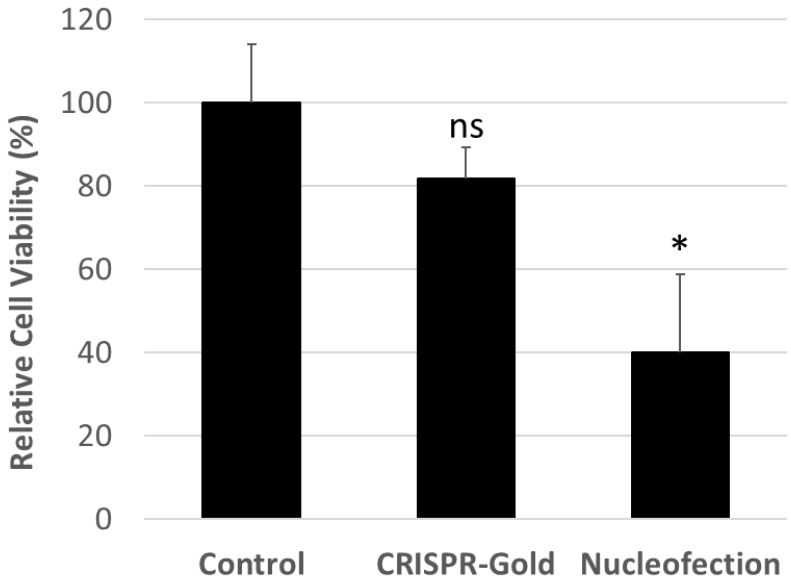

Figure 2.9. CRISPR-Gold is less toxic to hES cells than nucleofection. Nucleofection caused 60% cell death, 2 days after transfection, in contrast, CRISPR-Gold treated cells had a cell

viability comparable to the untreated control. Mean ± S.E, n=6. *, $p < 0.05$, ns = statistically not significant to the control.

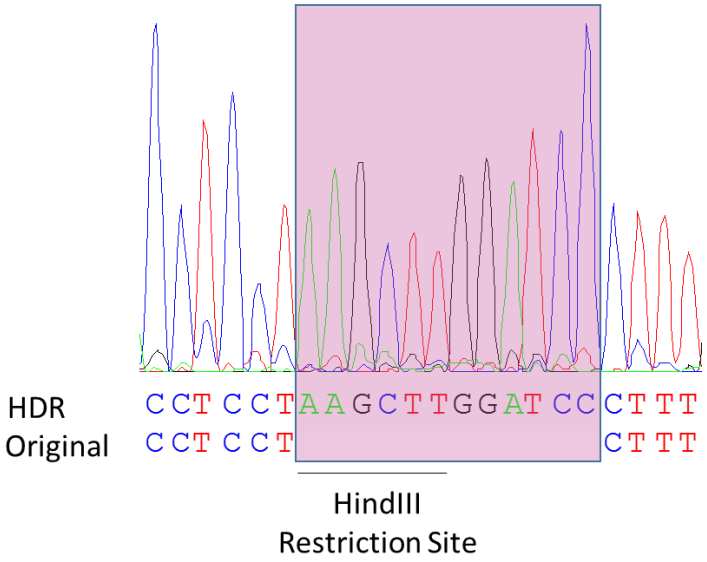

Figure 2.10. Sanger sequencing demonstrates that CRISPR-Gold induces HDR in hES cells. PCR of the CXCR4 gene was performed on CRISPR-Gold treated hES cells, and sequencing confirms the presence of the 12 bp insertion (pink box).

Additionally, we investigated if CRISPR-Gold could trigger HDR in cells grown in suspension, due to the importance of primary immune cells in cell therapy. Figure 2.11 shows that CRISPR-Gold induced efficient gene editing in mouse bone marrow-derived dendritic cells (BMDCs). These results suggest that CRISPR-Gold has the potential to edit the genome of primary cells and stem cells with high efficiency and accelerate the development of new cell-based therapies.

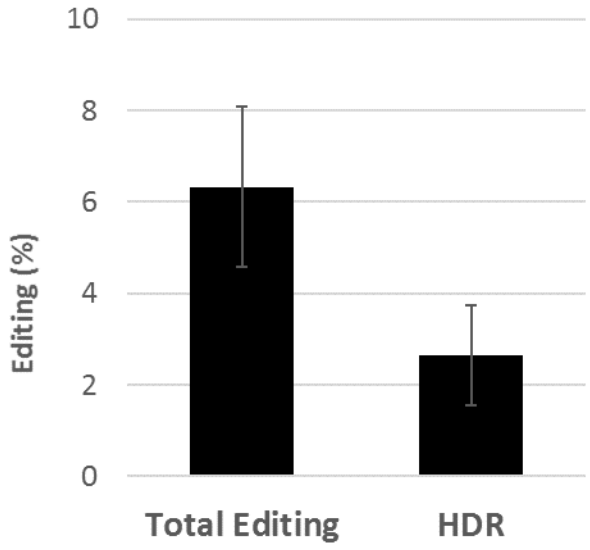

Figure 2.11. CRISPR-Gold induces genome editing in primary mouse bone marrow derived dendritic cells. CRISPR-Gold was incubated with dendritic cells isolated from mouse

bone marrow, using a guide RNA that targeted the dystrophin gene, and NHEJ and HDR were measured. CRISPR-Gold caused a total of 6% editing, which includes both NHEJ and HDR, and caused 3% HDR in dendritic cells. Mean ± S.E, n=3.

2.3.4 CRISPR-Gold testing in primary myoblasts from mdx mouse

CRISPR-Gold is a non-viral delivery vehicle that can edit genomes *via* HDR and has the potential to treat devastating genetic diseases caused by gene mutations. We decided to apply CRISPR-Gold for the treatment of Duchenne muscular dystrophy (DMD). First, we investigated if CRISPR-Gold could edit the dystrophin mutation in myoblasts *in vitro*, using myoblasts obtained from transgenic mice that have a non-sense mutation in the dystrophin gene frequently found in DMD patients (*mdx* mice)[15]. Myoblasts are the progeny of muscle stem cells (satellite cells), and are myogenic progenitor cells that are capable of proliferating and fusing with each other or with damaged muscle fibers, during the process of terminal myogenic differentiation[20]. Myoblasts are an excellent target for *in vivo* therapeutic applications of CRISPR-Gold because gene correction even in a small fraction of myoblasts *in vivo* may be sufficient to generate clinical benefits, due to the expansion of myogenic cells and the multinucleated nature of myofibers, which originate from the fusion of thousands of myoblasts. Primary myoblasts were derived from the satellite cells of cardiotoxcin (CTX) injured *mdx* mice. After 2-3 weeks in culture, these primary myoblasts were treated with CRISPR-Gold, which contained a guide RNA targeting the dystrophin mutation and a 180-mer ssODN that had the corrected dystrophin sequence[21]. Three days after CRISPR-Gold treatment, the correction of the dystrophin gene was determined *via* restriction enzyme analysis. Figure 2.12 demonstrates that CRISPR-Gold can efficiently deliver Cas9 RNP and donor DNA into primary myoblasts and induce HDR. For example, CRISPR-Gold treated myoblasts had an HDR efficiency of 3.5%, which was significantly better than either electroporation or lipofectamine. Importantly, CRISPR-Gold treated myoblasts had excellent cell viability (Figure 2.13).

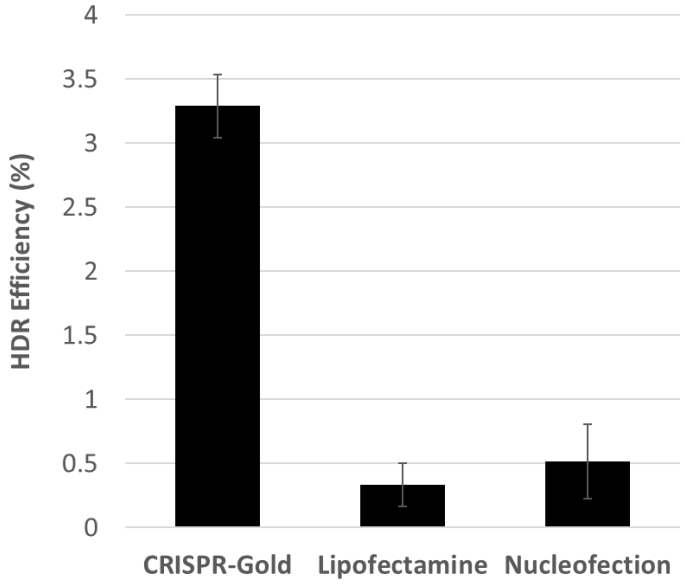

Figure 2.12. The dystrophin gene was efficiently edited with CRISPR-Gold in primary myoblasts from the *mdx* mouse. CRISPR-Gold corrected the nonsense mutation in the dystrophin gene of *mdx* myoblasts with an HDR efficiency of 3.3%, which is significantly higher than either nucleofection or lipofectamine. No correction was observed in the negative control,

composed of CRISPR-Gold without gRNA. Mean ± S.E, n=3. One-way ANOVA test had a p= 0.0002, which was statistically significant.

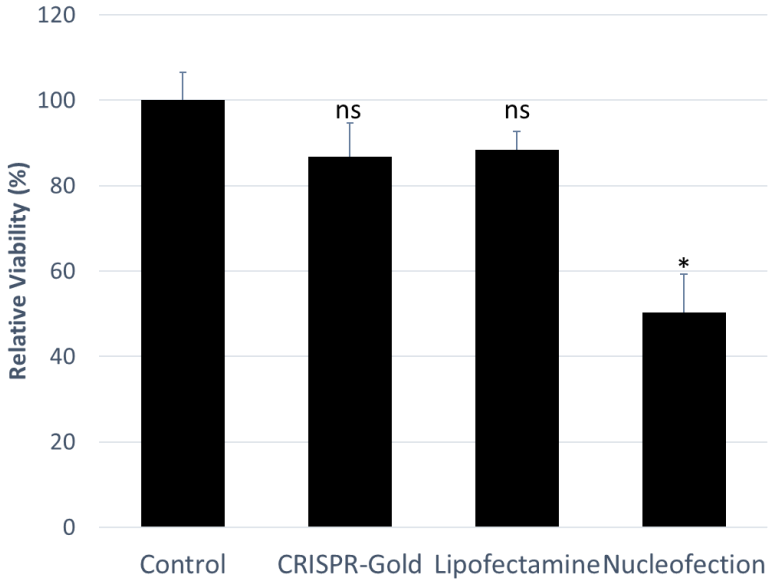

Figure 2.13. CRISPR-Gold causes minimal toxicity to myoblasts, whereas nucleofection caused significant levels of toxicity. Mean ± S.E, n=6. *, $p < 0.05$, ns = statistically not significant to control.

2.3.5 In vivo CRISPR-Gold test

Encouraged by the *in vitro* results, we investigated if CRISPR-Gold could correct the dystrophin mutation in *mdx* mice *in vivo* with a direct muscle injection. CRISPR-Gold and CTX were simultaneously injected into the hind legs of *mdx* mice, specifically, into their gastrocnemius and tibialis anterior muscles. Two weeks after the injection, the muscles were harvested and analyzed for dystrophin protein expression *via* immunohistochemistry and for correction of the dystrophin gene *via* deep sequencing (Fig. 2.14).

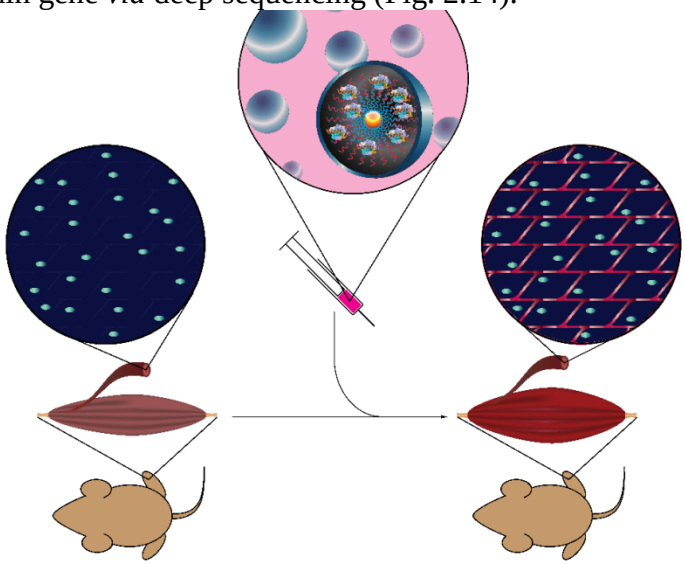

Figure 2.14. CRISPR-Gold efficiently delivers Cas9 RNP and donor DNA *in vivo* and restores dystrophin expression in *mdx* mice.
a) CRISPR-Gold was injected into the hind leg muscle of 8 week old mdx mice (n=3), simultaneously with CTX. Two weeks later, the mice were sacrificed and analyzed for dystrophin expression by immunofluorescence. The gastrocnemius and tibialis anterior muscles were dissected, sectioned to 10 µm, and immunostained for dystrophin protein.

Figures 2.15 and 2.16 show that CRISPR-Gold can correct the dystrophin mutation in *mdx* mice, and recover the expression of the dystrophin protein in muscle tissue after a direct injection. Robust dystrophin protein expression was observed in 10 µm cryo-sections of the muscles at the vicinity of the gold nanoparticles, and was significantly higher than the levels of dystrophin expression generally observed in 2 month old mdx mice, caused from spontaneous revertant fibers[22].

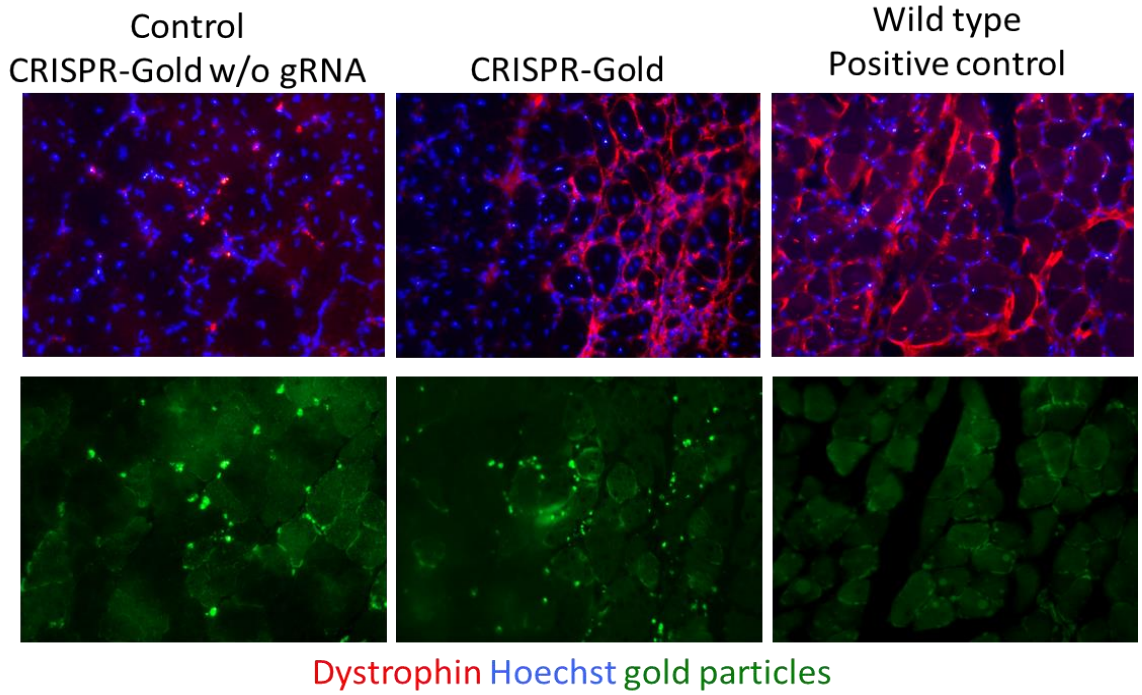

Figure 2.15. CRISPR-Gold causes dystrophin expression in muscle tissue of *mdx* mice. High magnification images (20x) of the injected muscle demonstrate dystrophin expression near the regions where gold nanoparticles are present (green fluorescence). Control mice that had been injected with CRISPR-Gold without gRNA had no evidence of dystrophin expression, despite the presence of gold nanoparticles. Positive control, wild-type mice robustly expressed dystrophin as expected. All nuclei appear blue (Hoechst staining). The width of each image is 1.4 mm.

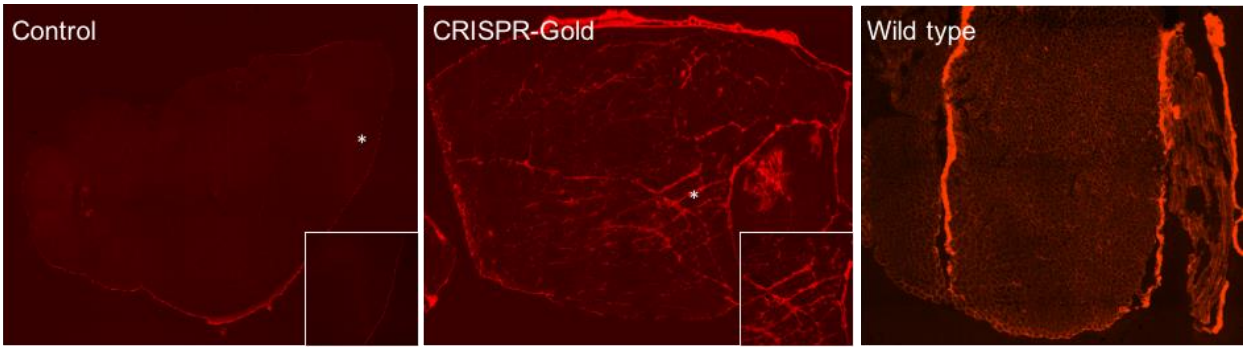

Figure 2.16. A representative montage image of CRISPR-Gold treated mice demonstrates that the whole muscle section shows dystrophin protein expression (red). Asterisk indicates the location of insets in the montage. Insets are 1.4 x 1.4 mm and the montage images have 5.6 mm width.

To further verify that CRISPR-Gold induced HDR in the dystrophin locus, PCR amplification of the corrected dystrophin gene was performed on both CRISPR-Gold treated *mdx* mice and control *mdx* mice that were injected with naked Cas9 RNP and Donor DNA. PCR amplification of the corrected dystrophin gene was only successful in the muscle treated with CRISPR-Gold. In addition, deep sequencing analysis was performed with DNA extracted from CRISPR-Gold injected muscle tissues and DNA extracted from muscle tissues injected with naked Cas9 RNP and Donor DNA. Figure 2.17 demonstrates that 5.4% of the CRISPR-Gold treated muscle genomic DNA had an exact sequence matching to the donor DNA sequence, whereas the control had only a 0.3% sequence match. Therefore, CRISPR-Gold can deliver Cas9 RNP and donor DNA to muscle tissue *in vivo* and efficiently induce HDR.

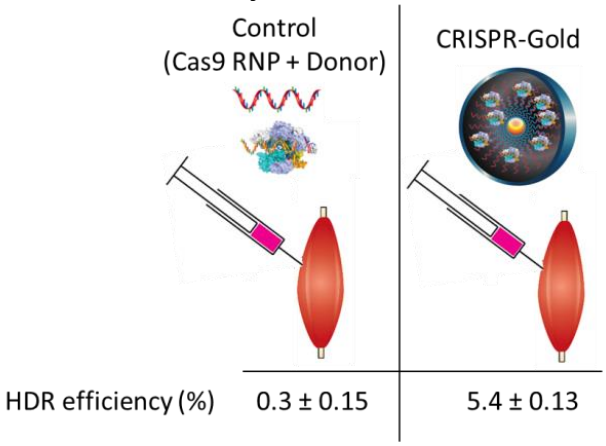

Figure 2.17. CRISPR-Gold induced dystrophin genome editing was confirmed by deep sequencing. Deep sequencing of genomic DNA from muscle tissues injected with CRISPR-Gold revealed a 5.4% HDR efficiency. The negative control composed of Cas9 RNP and donor DNA had an HDR efficiency of only 0.3%. Mean ± S.E, n=3.

Our data show that CRISPR-Gold can efficiently deliver Cas9 protein, guide RNA, and donor DNA both *in vitro* and *in vivo*. CRISPR-Gold represents the first example of a non-viral delivery vehicle that can induce HDR *in vivo* and thus holds great promise for the treatment of genetic diseases.

Chapter 3: *In vivo* delivery of transcription factors with multifunctional oligonucleotides

3.1 Introduction

The delivery of transcription factors is a central challenge in medicine. Transcription factors control every major physiological process within a cell, ranging from cell fate determination to inflammation resolution[23–25], and have the ability to correct the fundamental causes of a wide range of diseases. For example, the transcription factor Nuclear erythroid 2-related factor 2 (Nrf2) transcribes genes that resolve states of chronic oxidative stress and inflammation, and can protect against numerous incurable inflammatory diseases, such as atherosclerosis, Alzheimer's, and drug induced liver failure[26–28]. Therapeutics based on transcription factors, such as Nrf2, have tremendous therapeutic potential, but have been challenging to develop as therapeutics because of delivery problems[27,29,30]. The delivery of transcription factors is challenging because it requires developing a delivery vehicle that can complex transcription factors, target cells, and stimulate endosomal disruption, with minimal toxicity[31,32]. There is a great need for new transcription factor delivery vehicles[31,33].

3.2 Materials and Methods

3.2.1. Materials

3'-azide functionalized oligonucleotides were purchased from Intergrated DNA Technologies. All chemicals for the DART synthesis were purchased from Sigma-Aldrich. 0.1 M phosphate buffered saline (PBS), syringes, needles, pipette tips, eppendorf tubes, and nuclear magnetic resonance (NMR) tubes were purchased from VWR. ^{1}H-NMR spectra were recorded in $CDCl_3$, CD_3OD or D_2O on a Varian 400 spectrometer equipped with a Sun workstation at 300K. TMS (δ *(ppm)*$_H$ = 0.00) was used as the internal reference. ^{13}C-NMR spectra were recorded in either $CDCl_3$, CD_3OD and D_2O at a 100MHz on a Varian 400 spectrometer, using the central resonances of $CDCl_3$ (δ *(ppm)*$_C$ = 77.23) and methanol (δ *(ppm)*$_C$ = 49.15) as the internal references. Chemical shifts are reported in ppm and multiplicities are indicated by s (singlet), d (doublet), t (triplet), q (quartet), dd (doublet of doublets), and m (multiplet). Coupling constants, *J*, are reported in hertz (Hz). High-resolution mass spectra (HRMS) were obtained on a AB SCIEX TOF/TOF 5800 system and are reported as m/z (relative intensity). Accurate masses are reported for the molecular ion (M^+) or a suitable fragment ion. Chemicals were purchased from Aldrich or VWR and used without further purification. All solvents were purified using standard methods. Flash chromatography was carried out using silica gel (230-400 mesh). All reactions were performed under anhydrous conditions under N_2 or Argon and monitored by TLC on Kieselgel 60 F254 plates (Merck). Detection was accomplished by examination under UV light (254 nm) and by charring with 10 % sulfuric acid in methanol. The Nrf2 expression plasmid was obtained from Addgene (plasmid 21553). HepG2 cells and Hepa-1C1C7 were obtained from the biosciences divisional services at UC Berkeley. Female 6-8 weeks old C57BL6/J mice were purchased from Charles River.

3.2.2. Synthesis of the DARTs

The synthesis of the DARTs is shown in Figure 3.1. The key intermediate in the DART synthesis was the compound **5**, which is composed of a bivalent galactose, conjugated to a

hydrophobic C32 chain through an acid degradable acetal linkage. The compound **5** also contains a strained alkyne, which was used to conjugate to azide functionalized oligonucleotides, via copper-free click chemistry. A detailed description of the synthetic protocols used to generate **5** is described in Lee at al.[34].

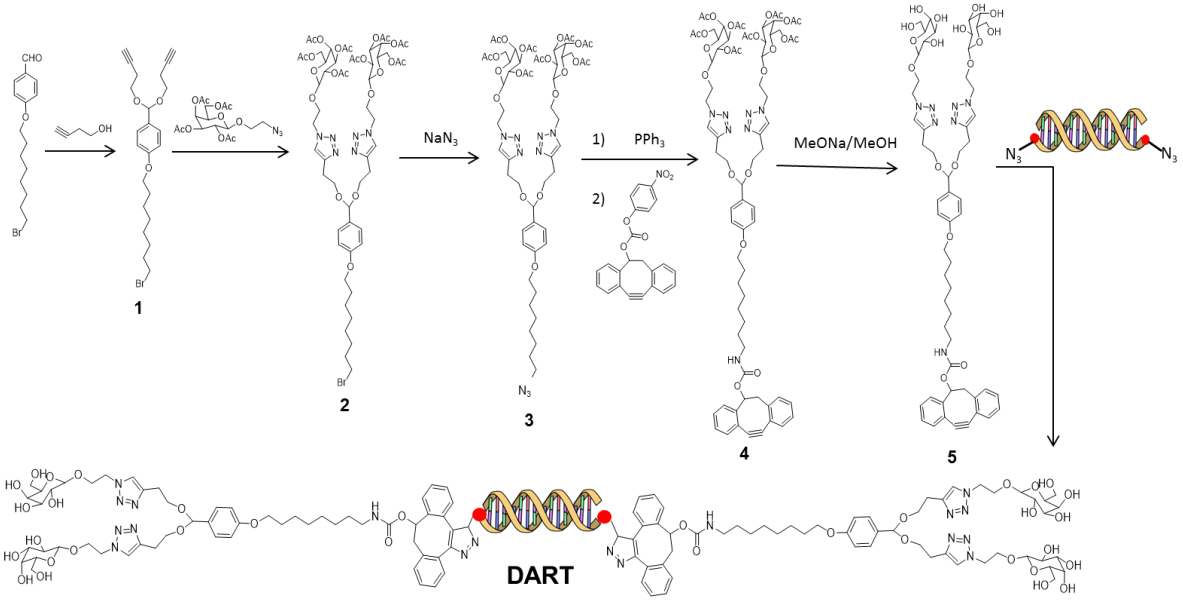

Figure 3.1. DART synthesis.
The DARTs were synthesized by conjugating 3'-azide functionalized oligonucleotides containing the Nrf2 ARE sequence, (forward strand 5'- GTC ACA GTG ACT CAG CAG AAT CTG TTT TT-N_3-3') and (reverse strand 5'- CAG ATT CTG CTG AGT CAC TGT GAC TTT TT-N_3-3'), with compound **5**, via copper free click chemistry. A 100 nmole of 3'-azide functionalized oligonucleotide and 600 nmole of compound **5** were mixed together in 10 µL of PBS (pH 10), incubated overnight at room temperature, and purified via a Bio-Spin 6 column. The conjugation of compound **5** to the individual oligonucleotides was determined by gel electrophoresis. The double stranded DARTs were generated by hybridizing equal molar ratios of the modified oligonucleotides**.** The oligonucleotides were incubated at 80 ℃ for 2 min in PBS (pH 10), were cooled down to room temperature for 30 min, and analyzed with gel electrophoresis.

3.2.3 Synthesis of Glu-DARTs

Glu-DARTs are identical to the DARTs, except that they contain glucose instead of galactose. The synthesis of the Glu-DARTs was accomplished via a procedure similar to that of the DARTs. Glu-DARTs were synthesized by conjugating 3'-azide functionalized oligonucleotides containing the Nrf2 ARE sequence, (forward strand 5'- GTC ACA GTG ACT CAG CAG AAT CTG TTT TT-N_3-3') and (reverse strand 5'- CAG ATT CTG CTG AGT CAC TGT GAC TTT TT-N_3-3'), with compound **9** via copper free click chemistry. A 100 nmole of 3'-azide functionalized oligonucleotide and 600 nmole of compound **9** were mixed together in 10 µL of PBS (pH 10), incubated overnight at room temperature, and purified via a Bio-Spin 6 column. The conjugation of compound **9** to the individual oligonucleotides was determined by gel

electrophoresis. Double stranded Glu-DARTs were generated by hybridizing equal molar ratios of the modified oligonucleotides**.**

3.2.4 Hydrolysis kinetics of DARTs

DART hydrolysis was investigated by gel electrophoresis. 1.5 μM of DART solutions were prepared in pH 5 and in pH 7.4 PBS solutions, incubated for various time points at 37 ℃, and then analyzed by gel electrophoresis using a 4-20% TBE polyacrylamide gel (Biorad) stained with ethidium bromide. The percent hydrolysis was determined by quantifying the bands comprising the intact and hydrolyzed DARTs, using ChemiDoc XRS (Bio-rad). Intact DARTs, DARTs with one acetal hydrolyzed, and DARTs with two acetals hydrolyzed were quantified. The percent hydrolysis of the DARTs was determined by integrating the two bands that represented DART hydrolysis products, one acetal hydrolyzed and both acetals hydrolyzed, and then dividing by the total DARTs present, which equaled the integration of the three bands corresponding to intact DART, one acetal hydrolyzed, and both acetals hydrolyzed. The one acetal hydrolyzed DART was multiplied by 0.5 to represent it as one acetal.

3.2.5 pH sensitive liposome leakage assay

Liposomes containing calcein (200 mg/mL) dye were prepared with DPPC (Dipalmitoylphosphatidylcholine) as previously described by Lorin et al.[12]. Liposomes were diluted in 100 μL of either pH 5 or 7.4 PBS solutions, in a 96-well plate. 10 μL of DART stock solutions at various concentrations were added to the liposomes to generate DART concentrations between 10 to 30 μg/mL in triplicate. The plate was shaken and the fluorescence was measured after 30 min of incubation (λ_{exc}=490 nm and λ_{ems}=515 nm). The negative control was PBS added to the liposomes, and the positive control was triton-X 100 (1 mg/mL). The percentage of calcein leakage was calculated according to the following equation:
% leakage = $(I_t - I_n) / (I_{max} - I_n)$ where I_t is the fluorescence intensity at 30 min after addition of DARTs, I_n the fluorescence intensity from the PBS negative control, and I_{max} the fluorescence intensity at 30 min after addition of triton-X 100.

3.2.6 Fluorescent labeling of Nrf2

500 μg of Nrf2 (500 μg/mL) was reacted with 5 times molar excess of Alexa555-NHS-ester, Alexa647-NHS-ester (Life Technologies), or IRDye 800CW-NHS-ester (LI-COR Biosciences) at 4 ℃ overnight in 0.1 M phosphate buffer (pH 8.5). A PD-10 column was used to remove unreacted Alexa dyes. The concentration of Nrf2 and conjugated Alexa555, Alexa647, or IRDye 800CW were measured with a Nanodrop 2000 (Thermo).

3.2.7 In vitro delivery of Nrf2 with DARTs

HepG2 cells were cultured in DMEM media containing 10% FBS and antibiotics (Pen Strep). Cells with a passage number less than 15 were used for experiments. HepG2 and Hepa-1C1C7 cells were seeded at 40% confluency the day before experiments. Nrf2 and DARTs were mixed at equal molar ratios and incubated for 15 min in binding buffer before the addition to cells. For all *in vitro* studies, 0.6 μM of Nrf2 or 0.6 μM of Nrf2 complexed with 0.6 μM of DARTs were

used. DARTs or Gal-DNA were mixed with Nrf2 at equal molar ratios and incubated in binding buffer for 15 min before addition to HepG2 cells. For all *in vitro* studies, 0.6 μM of Nrf2 or 0.6 μM of Nrf2 complexed with 0.6 μM of DARTs were used.

3.2.8 Intracellular localization of Nrf2 delivered by DARTs

The intracellular localization of Nrf2 delivered by the DARTs was observed by confocal microscopy (Swept Field Confocal microscope-Prairie Technology). Nrf2 was labeled with Alexa555 to visualize its intracellular localization. 500 μg of Nrf2 (500 μg/mL) was reacted with 9 times molar excess of Alexa555-NHS-ester (Life Technologies) at 4 ℃ overnight in 0.1 M phosphate buffer (pH 8.5). A PD-10 column was used to remove unreacted Alexa555. The concentration of Nrf2 and conjugated Alexa555 were measured with Nanodrop 2000 (Thermo). Alexa555-Nrf2 and DART were mixed at equal molar ratios and incubated for 15 min. HepG2 cells in 35 cm culture dishes were treated with 0.6 μM of Alexa555-Nrf2 prepared with or without DARTs for 30 min. After PBS wash, cells were incubated for additional 4 hr in culture medium. 100nM of Lysotracker Green DND-26 (Life Technologies) was added to the cells to visualize endosomes and lysosomes. HepG2 cells were washed with PBS and images were taken using confocal microscopy.

3.2.9 Delivery of Nrf2 *in vivo* with DARTs

For all the *in vivo* experiments, C57BL/6 female mice at 6 weeks of age were treated in accordance with the policies of the animal ethics committee of the University of California at Berkeley.

3.2.10 Treatment of acetaminophen (APAP) induced liver injury in mice with DART-Nrf2

After overnight fasting, mice were administered an intraperitoneal injection of APAP (500 mg/kg) dissolved in PBS (5% DMSO). One group of mice received free Nrf2 at the dose of 25 μg per mouse (1.25 mg/kg of Nrf2), and the other groups of mice were administered DARTs, DART-Nrf2, glucose-DART-Nrf2, and Gal-DNA-Nrf2 in 100 μL of PBS by tail-vein injection. 24 h after the injection of APAP, the mice were euthanized by CO_2 asphyxiation. The blood was collected by cardiac puncture and the livers were isolated. APAP-induced liver injury was determined by measuring the alanine aminotransferase (ALT) activity in the serum using a commercial ALT assay kit (Biovision). Liver samples were used for RNA isolation and histology to assess the liver damage. For histological analysis livers sections were stained by Hematoxylin and eosin, observed under light microscopy (Zeiss AxioCam ERc 5s), and the necrosis was compared between the groups of control, Nrf2 and DART-Nrf2 treated mice. Western blotting was performed with the liver samples to analyze the expression of HO1, NQO1, and GAPDH, using standard procedures. Transfer of proteins from liver homogenates to the nitrocellulose membrane (Bio-rad) was performed at 65V for 60 min. Primary antibodies (1:500) were incubated overnight at 4C and the secondary antibody, bovine anti-rabbit-HRP, (1:2000) was incubated for 2 hr at RT. Images were taken using a ChemiDoc XRS system (Bio-Rad Laboratories). HO1 antibody (sc-10789), NQO1 antibody (sc-25591), and bovine anti-rabbit IgG-HRP (sc-2370) were purchased from Santa Cruz Biotech.

3.2.11 Biodistribution of Nrf2 delivered by DARTs

Nrf2 was labeled with IRDye 800CW (LI-COR Biosciences) using the same procedure to conjugate the Alexa dyes as described in S7. Mice were intravenously injected with either free Nrf2 or DART-Nrf2 (1.25 mg/kg of Nrf2 and 0.423 mg/kg of DARTs in a 100 μL of PBS). Mice were euthanized by CO_2 asphyxiation 4 h after injection and the liver, lung, heart, kidney, spleen, and brain were harvested. Ex vivo imaging of organs was performed using an IVIS imaging system. IRDye fluorescence from the organs was quantified. Briefly, the organs were homogenized in 1 mL of PBS, and centrifuged at 13,000 g for 30 min. IRDye fluorescence intensity in 100 μL of the supernatant was quantified using a plate reader ($\lambda_{ex}/\lambda_{em}$=760/800; Tecan). To correct for background fluorescence, the fluorescence from control organs was subtracted from the fluorescence measured in the organs of Nrf2 or DART-Nrf2 treated mice.

3.2.12 Serum TNF-α analysis of mice treated with DARTs

Mice were administered free Nrf2, DART-Nrf2, or DARTs, at a dose of 5 mg/kg of Nrf2 and 1.69 mg/kg of DARTs. 24 h after administration of the samples, the blood was collected by cardiac puncture. Serum TNF-α levels were measured with a mouse TNF-α ELISA kit (eBioscience) following the manufacturer's instruction. The control mice for this experiment were untreated mice.

3.2.13 Statistics

Statistical analyses were performed using a student t-test and p-values for each experiment were determined. Statistically significant data ($p<0.05$) are depicted using the '*' symbol and $p<0.01$ data are depicted using the '**' symbol.

3.3. Results and Discussion

3.3.1 The Design of DARTs

We designed a transcription factor delivery vehicle, termed DARTs (DNA Assembled Recombinant Transcription factors), which can deliver Nrf2 to the liver and rescue mice from acute liver failure. The chemical structure of the DARTs and the mechanism by which they are designed to deliver transcription factors are shown in Figure 3.2. DARTs are composed of an oligonucleotide that contains an Nrf2 binding sequence and hydrophobic C32 alkyl chains that are "masked" by acid cleavable galactose residues, which are conjugated via acetal linkages[35]. The DARTs are able to complex Nrf2 because they contain an Nrf2 promoter sequence, which binds Nrf2 with high affinity, and can also target hepatocytes because they have galactose conjugated to their 3' ends. In addition, the unique molecular architecture of the DARTs allows them to be pH sensitive membrane disruptive agents, and disrupt endosomes efficiently with minimal toxicity. The DARTs are designed to have minimal toxicity while they are circulating in the blood, because at pH 7.4, their hydrophobic domains are unable to interact with cell membranes due to the adjacent galactose groups. However, after endocytosis, the galactose groups of the DARTs are cleaved as a result of hydrolysis, and this activates the hydrophobic domains and allows them to disrupt the endosomal membrane.

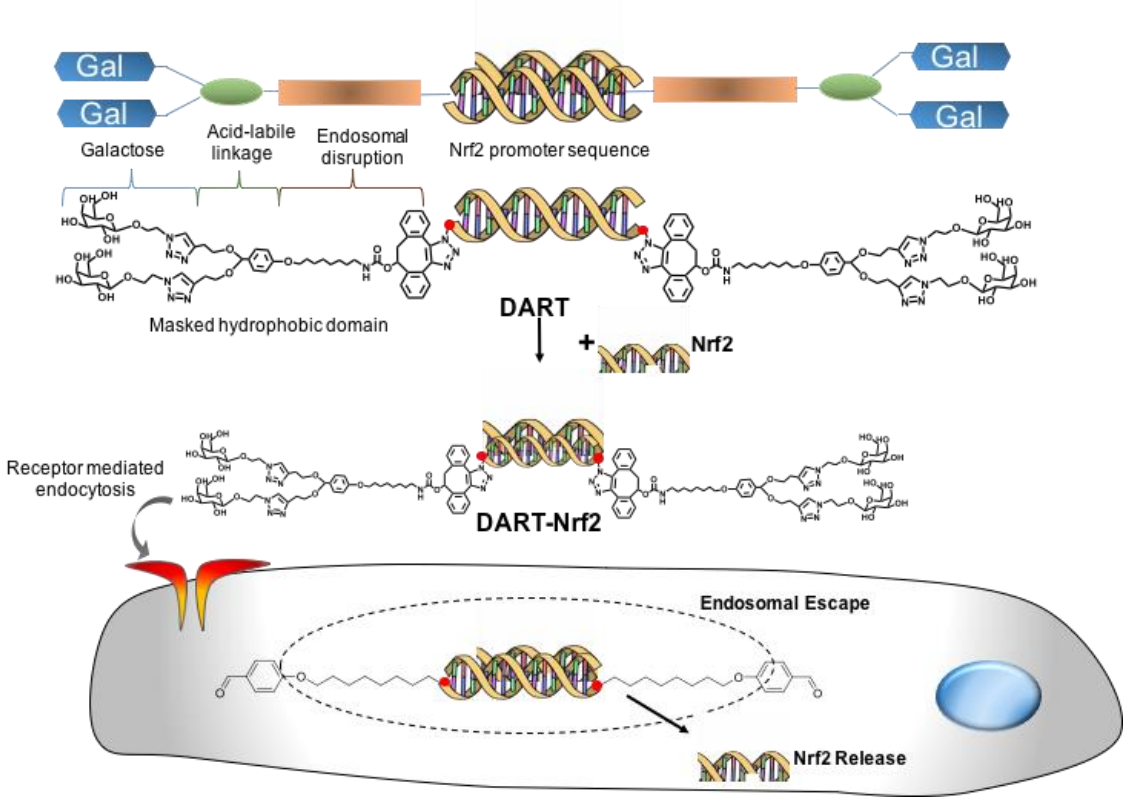

Figure 3.2. DARTs are multifunctional oligonucleotides that can deliver the transcription factor Nrf2 *in vivo*.
DARTs are composed of an oligonucleotide that contains an Nrf2 promoter sequence and hydrophobic membrane disruptive domains that are masked by acid cleavable galactose residues. DARTs complex Nrf2 and deliver Nrf2 to the liver via galactose mediated endocytosis. After

endocytosis, DARTs stimulate endosomal disruption and the release of Nrf2 into the cytoplasm, due to acid catalyzed unmasking of their hydrophobic domains.

The DARTs are designed to address several key challenges associated with delivering transcription factors *in vivo*. For example, transcription factors can be delivered via the DARTs by simply mixing them together. In contrast traditional protein delivery strategies require chemical modification of the protein or exposure to organic solvents, both of which frequently cause protein denaturation or the generation of antigenicity[31]. DARTs are well-defined molecules that can also be synthesized on a large scale, and avoid the characterization and manufacturing problems associated with self-assembled systems. In addition, DARTs are able to disrupt endosomes without using cationic peptides or polymers and thus overcome the toxicity problems associated with traditional endosomal disruptive strategies[36]. Finally, the DART delivery strategy is modular, and a variety of transcription factors can potentially be delivered via the DART strategy by simply changing their oligonucleotide sequence and targeting moieties.

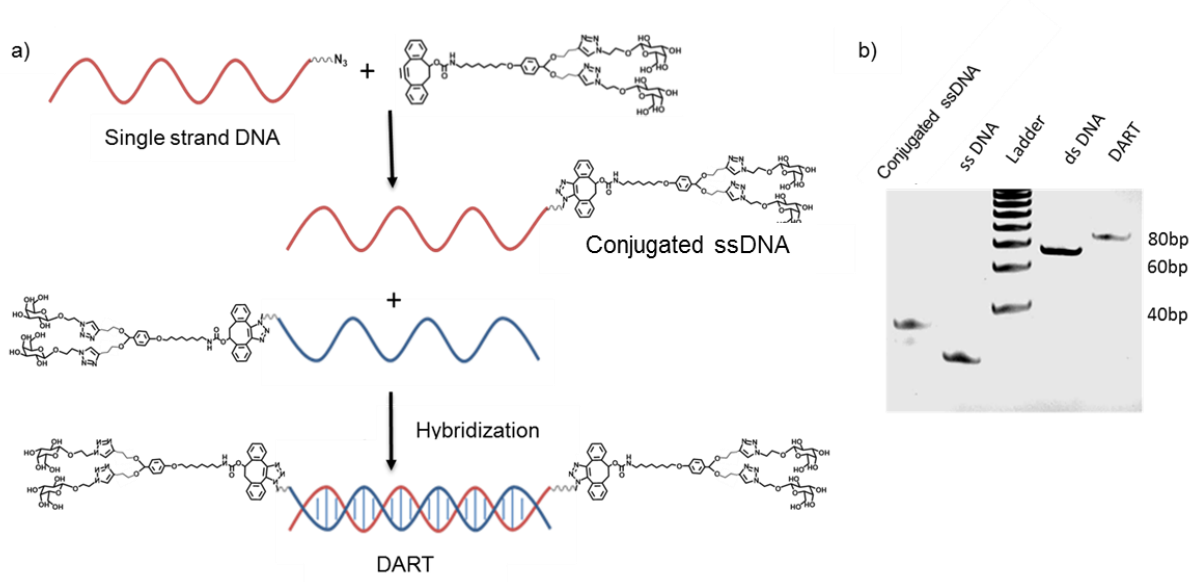

Figure 3.3. Conjugation of compound 5 to azide-modified oligonucleotides.
a) DARTs were synthesized by conjugating azide-modified oligonucleotides containing the Nrf2 consensus sequence with compound **5**, followed by hybridization.
b) Characterization of DART synthesis. Polyacrylamide gel electrophoresis confirms the conjugation of **5** to ssDNA, as evidenced by the mobility shift in the ssDNA conjugate lane. ssDNA conjugate lane migrates slower than unmodified DNA. Similar changes in mobility were seen between DART and dsDNA.

3.3.2 Characterization of DARTs

The pH sensitive hydrolysis of the acetal linkage in the DARTs is a critical feature of their molecular design. The DARTs need to be stable at pH 7.4 to allow for circulation in the blood with low toxicity, but hydrolyze rapidly at pH 5.0 and trigger endosomal disruption, before extensive degradation in the lysosome occurs. The hydrolysis kinetics of the DARTs was measured at pH 5.0 and pH 7.4, via gel electrophoresis. Figure 3.4 demonstrates that DARTs undergo pH sensitive hydrolysis with an estimated half-life of 41 minutes at pH 5.0, but have an

estimated half-life of 12 hours at pH 7.4. Intravenously injected galactose containing molecules are internalized by the liver within 1 hour[37], and the pH 7.4 hydrolysis kinetics of the DARTs should be suitable for delivering transcription factors to the liver. In addition, the rapid hydrolysis of the DARTs at pH 5.0, suggests that they will trigger endosomal escape before extensive degradation of Nrf2 in the lysosomes occurs.

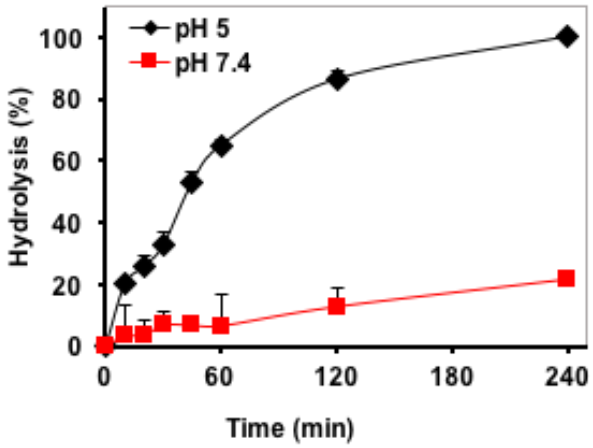

Figure 3.4. The hydrolysis of the DARTs is acid catalyzed. DART hydrolysis was conducted at pH 5 and pH 7.4 PBS, ± S.E, n=5.

The acid catalyzed hydrolysis of the DARTs is designed to trigger endosomal disruption via unmasking of their hydrophobic domains. We therefore investigated if DARTs could disrupt liposomes in a pH sensitive manner using a calcein leakage assay. DARTs were incubated with calcein containing liposomes at either pH 5.0 or 7.4 for 30 minutes, at concentrations between 10 - 30 μg/mL, and the disruption of liposomes was measured via the increase in calcein fluorescence. Figure 3.5 demonstrates that DARTs have pH sensitive membrane disruptive properties, and can disrupt lipid bilayers in an efficient manner. For example, calcein containing liposomes incubated with DARTs at a 20 μg/mL (1 μM) concentration at pH 5.0 released approximately 40% of their encapsulated calcein in 30 minutes, whereas liposomes incubated at pH 7.4 released only 10% of their encapsulated calcein. DARTs have a membrane disruptive capacity similar to commonly used endosomal disruptive polymers, such as co-polymers of diethylaminoethyl methacrylate and butyl methacrylate, which also require μg/mL concentrations to disrupt membranes, and this suggests that the DARTs will be able to enhance the cytoplasmic delivery of transcription factors[17].

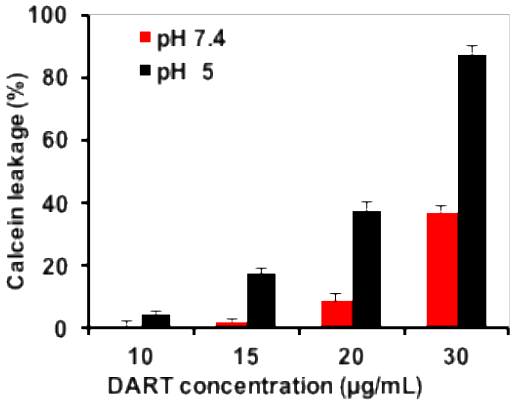

Figure 3.5. **DARTs disrupt calcein containing liposomes in a pH-dependent manner.** Liposome disruption by the DARTs was assessed by calcein leakage, mean ± S.E, n=5. **, $p < 0.01$.

3.3.3 *In vitro* test of DARTs in HepG2 cells

We performed fluorescent microscopy experiments to determine if DARTs could enhance the endosomal release of Nrf2. HepG2 cells were treated with DART-Alexa555-Nrf2 complexes and the intracellular localization of Nrf2 was investigated via confocal microscopy, using Lysotracker green to mark endosomes and lysosomes. Figure 3.6 demonstrates that DARTs can dramatically alter the intracellular distribution of Nrf2, and causes a significant fraction of the delivered Nrf2 to localize in compartments distinct from lysosomes. In contrast, free Nrf2 is mostly found in lysosomes.

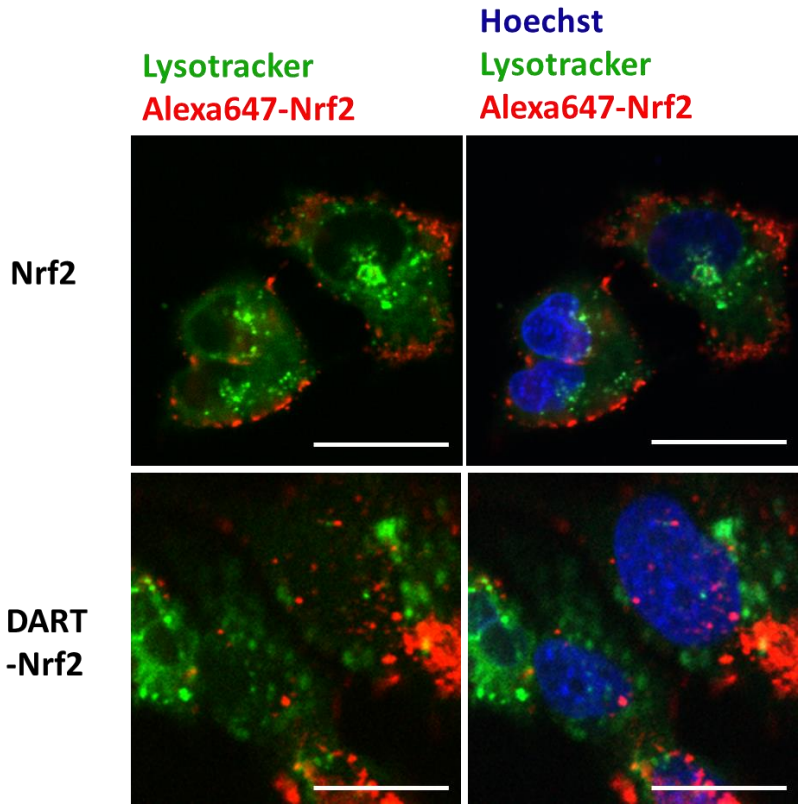

Figure 3.6. DARTs alter the intracellular delivery of Nrf2 and enhance lysosomal release. Alexa555 labeled Nrf2 (red color) was complexed with the DARTs and incubated with HepG2 cells. Endosomes were counterstained with Lysotracker green (green color). Nrf2 complexed with the DARTs have a substantially different intracellular distribution than free Nrf2, with a large fraction existing outside of the lysosome, whereas free Nrf2 is predominantly in lysosomes. (Scale bar: 5 μm).

3.3.4 *In vivo* biodistribution study

DARTs contain a tetravalent galactose group for hepatocyte targeting. We performed *in vivo* biodistribution and pharmacokinetic experiments with Nrf2 complexed with DARTs, to determine if the DARTs could enhance the accumulation of Nrf2 in the liver. Figure 3.7 demonstrates that the DARTs can increase the delivery of Nrf2 to the liver, causing an approximately 1.4 fold increase in liver delivery compared to free Nrf2, suggesting that the galactose targeting via the DARTs increases the delivery of Nrf2 to the liver. In addition, no evidence of systemic toxicity was observed in mice injected with Nrf2 complexed with the DARTs, as determined by blood TNF-α levels (Fig. 3.8).

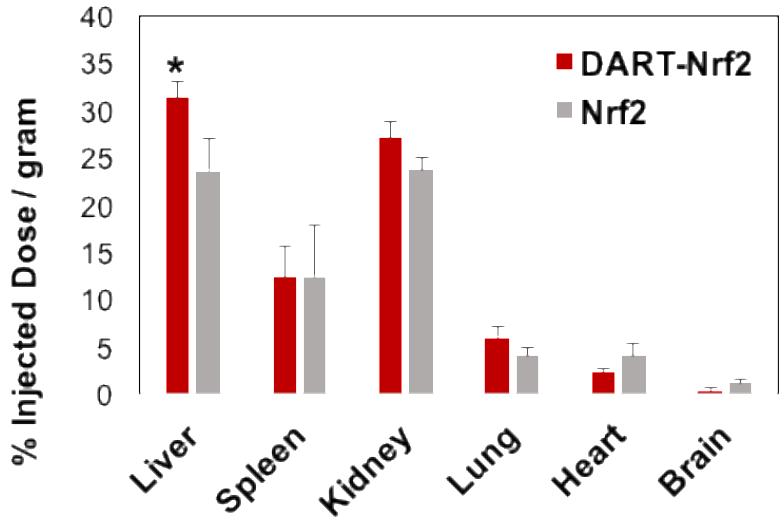

Figure 3.7. The DARTs can target hepatocytes and enhance the delivery of Nrf2 to the liver. Nrf2 labeled with IR Dye was complexed with the DARTs, and injected into mice. The biodistribution of Nrf2 was quantified via fluorescence 4 hours after Nrf2 injection. DARTs enhance the liver delivery of Nrf2 by a factor of 1.4. mean ± S.E, n=6. *, $p < 0.05$.

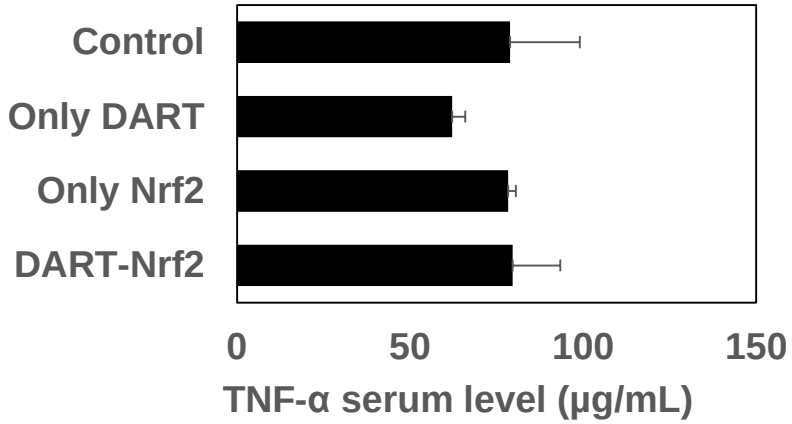

Figure 3.8. DARTs cause minimal inflammation *in vivo*. The serum levels of TNF-α were not significantly altered in mice treated with DARTs, Nrf2, or DART-Nrf2 versus untreated controls, mean ± S.E, n=3, all samples are statistically not significant to control.

3.3.5. DART-Nrf2 treatment in APAP induced liver injured mouse

Nrf2 delivered by DARTs has great potential for treating liver associated inflammatory diseases, such as acute liver failure and liver fibrosis, which collectively effect millions of people each year[27,29,30]. We investigated if Nrf2 delivered by DARTs could protect mice against acetaminophen (APAP) induced liver injury. APAP induced liver injury was selected as an initial disease model for the DARTs because of the great need for new therapeutics against this disease and the well-established role of Nrf2 in protecting against APAP induced liver injury[38,39]. APAP induced toxicity in mice was induced via the i.p. injection of APAP (500mg/kg), and 1 hour afterwards an intravenous injection of either free Nrf2 or DART-Nrf2 was given. Liver toxicity was determined 24 hours later by measuring ALT levels in the serum and also via histology. Additionally, liver tissue was isolated from these mice and analyzed by western blotting to determine if Nrf2 delivered by the DARTs could induce the expression of Nrf2 downstream genes.

Figures 3.8-3.10 demonstrate that DARTs can enhance the delivery of Nrf2 *in vivo*, induce the transcription of Nrf2 downstream genes, and protect mice from APAP induced liver injury. For example, Figure 3.8 demonstrates that mice receiving DART-Nrf2 and APAP had a four-fold decrease in ALT levels in comparison to mice that received APAP only, or mice that received APAP and free Nrf2. A similar therapeutic benefit was observed in the histology sections of the mice that received DART-Nrf2 and APAP, which had a histological profile similar to healthy mice; in contrast mice receiving free Nrf2 and APAP had significant signs of toxicity (Fig. 3.9). Importantly, DART-Nrf2 was able to have a therapeutic effect on APAP treated mice, even though it was given an hour after APAP administration, suggesting that it can be effective in a clinical scenario where patients present hours after drug intake.

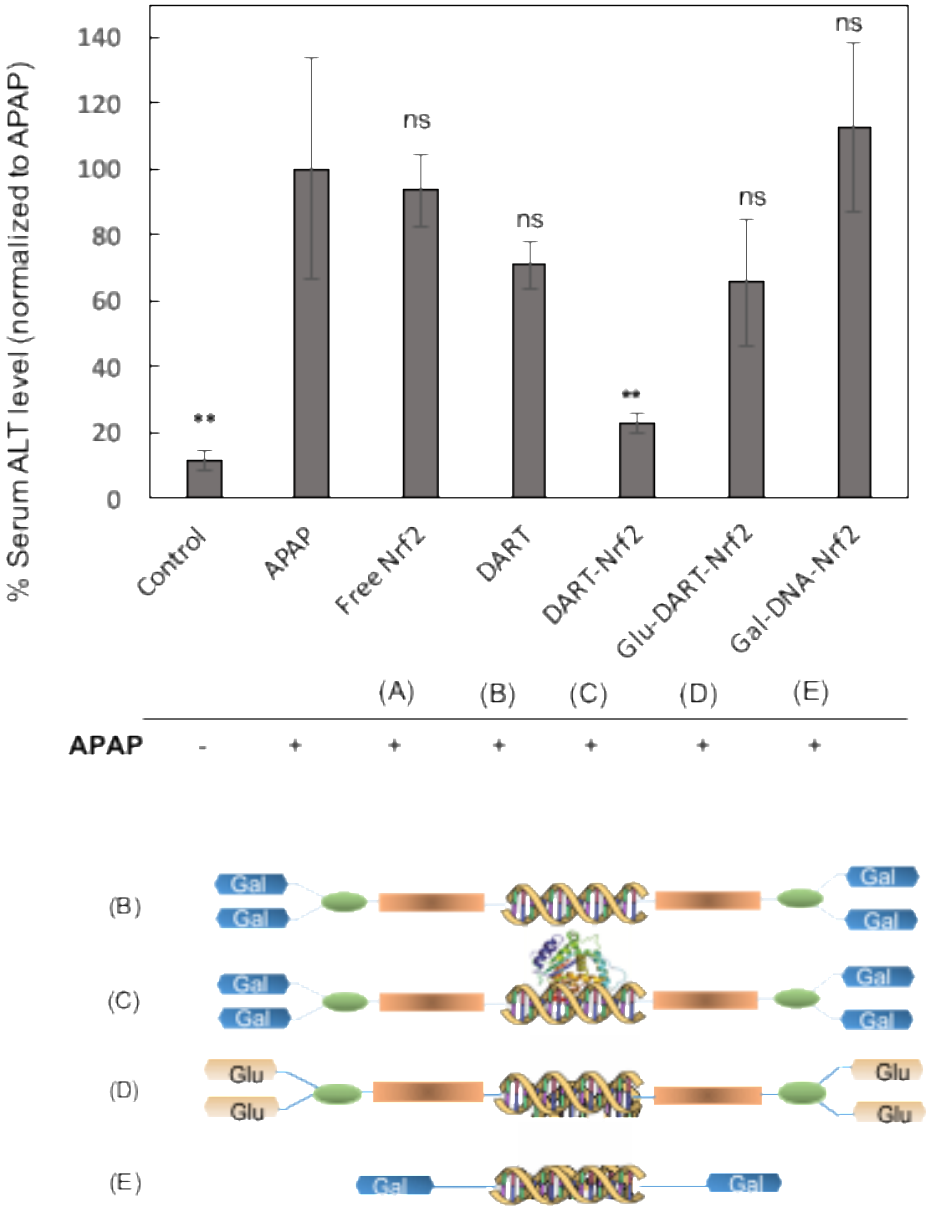

Figure 3.8. Nrf2 delivered by DARTs rescue mice from acetaminophen (APAP) induced liver injury. DART-Nrf2 complexes reduce serum alanine transaminase (ALT) levels in APAP treated mice by a factor of 4. Free Nrf2 had no effect. Nrf2 complexed with either Glu-DARTs or Gal-DNA, and free DARTs, did not cause a statistically significant reduction in ALT levels. mean ± S.E, n=10. $p < 0.01$, ns = statistically not significant to APAP.

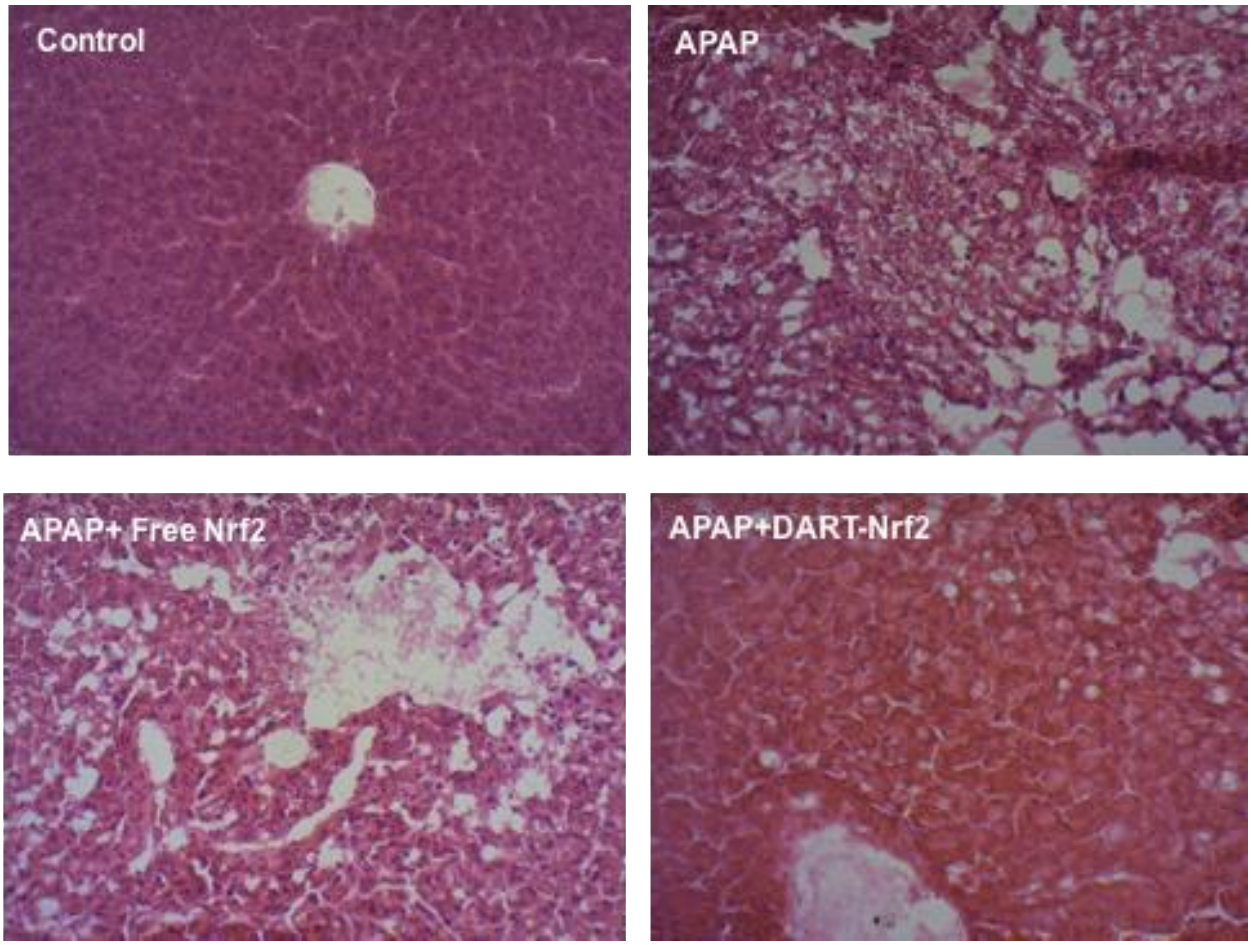

Figure 3.9. Nrf2 delivered by DARTs reduces liver damage in APAP treated mice. Histological sections of livers from APAP treated mice had significant inflammation. In contrast, histological sections of livers from APAP mice treated with DART-Nrf2 had reduced liver damage and resembled the histological sections of healthy mice. Free Nrf2 was unable to suppress liver damage. (Scale bar: 40 μm).

In addition, we investigated if Nrf2 complexed with DARTs could stimulate the transcription of Nrf2 downstream genes *in vivo*, via western blotting for the Nrf2 downstream genes HO1 and NQO1. Figure 3.10 demonstrates that Nrf2 delivered by the DARTs can increase the expression of HO1 and NQO1 in the liver, and suggests that the therapeutic effects of DART delivered Nrf2 are due to the enhanced transcription of Nrf2 downstream genes.

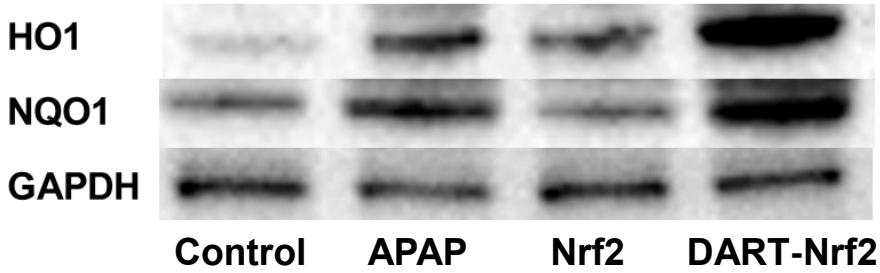

Figure 3.10. Nrf2 delivered by DARTs enhances the expression of the proteins HO1 and NQO1 in the liver. APAP treated mice were given either DART-Nrf2 or free Nrf2, and their livers were harvested and western blot analysis was conducted for the proteins HO1, NQO1, and GAPDH. Mice treated with Nrf2-DART complexes have increased HO1 and NQO1 expression in comparison to free Nrf2 or APAP treated mice. Control = no treatment, APAP = APAP only, Nrf2 = APAP+Nrf2, DART = APAP+DART-Nrf2.

Here, we present a novel multifunctional oligonucleotide, termed DARTs, which can deliver transcription factors with high efficiency *in vivo*. DARTs are composed of an oligonucleotide that contain a transcription factor binding sequence and hydrophobic membrane disruptive chains that are masked by acid cleavable galactose residues. DARTs have a unique molecular architecture, which allows them to bind transcription factors, trigger endocytosis in hepatocytes, and stimulate endosomal disruption. The DARTs target hepatocytes as a result of the galactose residues and can disrupt endosomes efficiently with minimal toxicity, because unmasking of their hydrophobic domains selectively occurs in the acidic environment of the endosome. We show here that DARTs can deliver the transcription factor Nrf2 to the liver, catalyze the transcription of Nrf2 downstream genes, and rescue mice from acetaminophen induced liver injury.

Chapter 4. Shape effect in the design of nanowire-coated microparticles as transepithelial drug delivery devices

4.1 Introduction

The ability to control shape, size and interfacial properties to enhance the functionality of particle-based drug delivery devices is increasingly being recognized[40]. By means of controlling the particle topography, the interfacial energy between the device and the adjacent tissue and the biological response of the latter can be controlled[41–43]. Elongated and asymmetrical particles in particular present a convenient choice for drug delivery devices intended to adhere onto a biological surface[44,45]. Highly irregular, discoid and cylindroid particles were, for example, shown to adhere to tumor vasculature and be sequestered by the liver, spleen and lung to a much greater extent than spherical particles did[46]. This shape effect has been already utilized by some biological compounds, including cholesterol platelets and elongated calcium phosphate crystals that comprise atherosclerotic plaque[47]. Namely, their effective adherence onto blood vessel walls is owing to their propensity to form planar particles and thus maximize the surface area in contact with the tissue[48].

There are a number of challenges in oral drug delivery[49–51], including (a) the harsh acidic environment in the gut, (b) rapid clearing of the drug off the epithelial lining, and (c) the finite size limit, ~ 300 Da[52], for the paracellular transport of the drug from the intestines and into the bloodstream. Nanotopology strategies can be applied in the design of oral drug delivery carriers whose purpose is to adhere strongly onto the target tissue and resist being carried away by the microflows of the mucous layer[40].

In former studies, people showed that microsized silica beads coated with silicon nanowires present good candidates for adhesive drug delivery devices due to: (a) the facility of their loading with drug suspensions via the capillary effect[53]; (b) their ability to entwine with and sterically adhere to apical microvilli on the surface of epithelial cells[54,55]; and (c) their ability to increase the tight junction (TJ) permeability and enable a more effective passage for the small molecule drugs across the *in vitro* model of the epithelium[56].

In this study, we modified the shape of the microparticles onto which nanowires are attached from spherical to planar and analyzed the effects of this microscale morphological variation on the permeability of the epithelium formed *in vitro* by Caco-2, a human colon carcinoma cell line, and *in vivo*.

4.2. Materials and Methods

4.2.1 Spherical and planar silica microparticles coated with nanowires

Spherical (S) and planar (P) silica microparticles were provided by Nanosys, Inc., in two forms: bare (S_B, P_B) and coated with silicon nanowires (S_{NW}, P_{NW}). The particles were synthesized by means of chemical vapor deposition of silicon ions onto silica microparticles sputtered with gold. Scanning Electron Microscopy (SEM, Hitachi, S-4300SE/N) was used for the morphological and size analysis of the four types of particles utilized in this study.

4.2.2 Caco-2 Cell Culture

The human intestinal Caco-2 cells were obtained from American Tissue Culture Collection (ATCC, Rockville, MD) and cultured in Eagle's Minimum Essential Medium with Earle's Balanced Salt Solution, 1 mM sodium pyruvate, 20% fetal bovine serum (Sigma), and 1% penicillin-streptomycin antibiotic solution. In all experiments, the cells were seeded in 24 well plates at a density of 7.5 x 10^4 cells/well on either collagen-coated glass cover slips (Fisherbrand®) or in the apical compartments of Transwells™. Every 7 days, the cells were detached from stock cultures by means of trypsin (0.25 wt%) digestion, washed, centrifuged (1000 rpm x 3 min), resuspended in 10 ml media and subcultured in 1:7 volume ratio. The cultures were regularly examined under an optical microscope to monitor their growth and possible contamination. Cell passages 22 – 35 were used for the hereby reported experiments.

4.2.3 Drug loading and elution

Solvent-evaporation-induced capillary effect was used as a mechanism for loading the particles with the moderately sized model drug, insulin. Two milligrams of microparticles were immersed in 166 µl of the loading solution and heated at 35 °C for approximately 24 h (until dry). The loading solution comprised 10 mg/ml of bovine pancreatic insulin (Sigma) dissolved in phosphate buffer saline (PBS). To remove the residual, unloaded drug, washing with PBS was carried out, after which the particles were transferred to a new vial and weighed. Particles loaded with insulin were suspended in 0.5 ml of PBS and kept on a shaker plate for 4 h. A portion of the supernatant (25 µl) was periodically extracted to quantify the amount of eluted insulin. The quantification was performed using a regular bicinchoninic acid (BCA) protein assay. The absorbance of the samples was read at λ = 562 nm following the manufacturer's guidelines.

4.2.4 Drug permeability across Caco-2 cell monolayers

Confluent Caco-2 cells seeded in high-density cell culture inserts with 0.4 µm pore size (Falcon®) placed in 24 well plates were exposed apically to 2 – 20 mg of particles (S_B, P_B, S_{NW}, P_{NW}) in 500 µl of the phenol-free cell culture media. The basolateral compartments initially contained 1ml PBS. Separate permeability experiments were carried out (a) with insulin-loaded microparticles and (b) with microparticles and separately added 1 mg/ml solutions of drugs of various sizes: 389 Da fluorescein isothiocyanate (FITC) and 5.6 kDa insulin. FITC was applied as a sodium salt and thus permeated the cell layers in ionized form. A portion of the supernatant (25 µl) was periodically extracted from the basolateral compartment to quantify the amount of eluted drug using either BCA assay or a Packard Fluorocount™ fluorometer at the excitation λ = 495 nm and the emission λ = 518 nm. All the experiments were done in triplicates and each experimental replica was analyzed for the drug content also in triplicates (n = 3 x 3). The initial TEER was between 600 and 1000 Ωcm^2, matching the earlier reported range of values for polarized monolayers of confluent Caco-2 cells and the epithelial lining of the colon[57,58]. The permeability coefficients (P_{app}) for different fluorescent drugs were calculated using the following equation[59], in which dq/dt is the rate of change in the amount of fluorescence on the basolateral side converted to fluorophore concentration units (mg/ml), *A* is the surface area of the inserts, and C °is the initial concentration of fluorophore applied in the apical compartment (mg/ml):

$$P_{app} = \frac{dq}{dt} \times \frac{1}{A \times C^{\circ}} \qquad \text{(Eq.1)}$$

4.2.5. Immunofluorescence for zonula occludens-1 (ZO-1)

Upon reaching full confluency, Caco-2 cells in 24 well plates were treated with different amounts of S_{NW} and P_{NW} particles (4, 10 or 20 mg per well) suspended in 500 µl of the cell culture media, and incubated for 4 h at 37 ^{o}C. The media along with the particles were then aspirated and the cells were washed with PBS and fixed for either 5 min in – 20 ^{o}C methanol. The cells were then washed three times with PBS, 5 min each, and then with the blocking solution (PBT = 1 % BSA, 0.1 % Triton X-100 in PBS) two times, 5 min each. The cells were then blocked and permeabilized in PBT for 1 h and incubated with 200 µl/well primary antibody, 10 µg/ml rabbit anti-ZO-1 (Zymed Lab) in PBT overnight at 4 ^{o}C. After the overnight incubation, the cells were washed with PBS 3 x 10 min and then incubated with 150 µl/well secondary antibody, 2.5 µg/ml AlexaFluor 555 goat anti-rabbit IgG (Invitrogen) and 20 µg/ml 4',6-diamidino-2-phenylindole dihydrochloride nuclear counterstain (DAPI, Invitrogen), all in PBT for 1 h at room temperature. After washing with PBS 3 x 5 min, the cover slips containing the fixed and stained cells were mounted onto glass slides using vectashield and nail hardener and imaged in oil under a confocal laser scanning microscope – C1si (UCSF Nikon Imaging Center) at 60 - 100 x magnification. All the experiments were done in triplicates and the staining immunofluorescence pixel intensity was measured from four randomly selected images in each sample (n = 4 x 3). Volume-rendered z-stack images (12 – 15 of them) spaced by 1 µm were collected at identical laser intensities and analyzed for the fluorescence intensity, the thickness of ZO-1 conglomerates and the percentage of the ruffled TJ pattern using ImageJ and NIS Elements software. The thickness of ZO-1 conglomerates at the tight junction was measured as half-width of peaks obtained by plotting the fluorescence intensity profiles across the cell boundary.

4.3. Results and discussion

4.3.1 Planar particle synthesis

The shape of P particles was rationally designed with a two aims: (a) to maximize the duration of adhesion to the mucous epithelium of intestines under high shear flow, and (b) to increase the surface area in contact with the epithelium. In the oral delivery platform, the drug permeability and the residence time of the delivery device in intestines are two key factors determining their therapeutic effectiveness.

SEM images of four types of particles utilized in this study are shown in Fig. 4.1: bare spherical (S_B) and planar (P_B) silica microparticles and nanowire-coated spherical (S_{NW}) and planar (P_{NW}) silica microparticles. Spherical particles were narrowly dispersed with a diameter of 30 – 50 µm. Planar microparticles were less regularly shaped, but equally narrowly dispersed, with the average dimensions of 100 x 50 x 5 µm. Aside from their larger surface area in comparison with S particles, they also possessed a more asymmetric planar geometry, intended to facilitate adhesive interaction with the epithelium. The average length of nanowires grown from the particle surface was 4 – 8 µm for S_{NW} and 5-10 µm for P_{NW}. For both particles, the diameter of the nanowires was circa 60 nm.

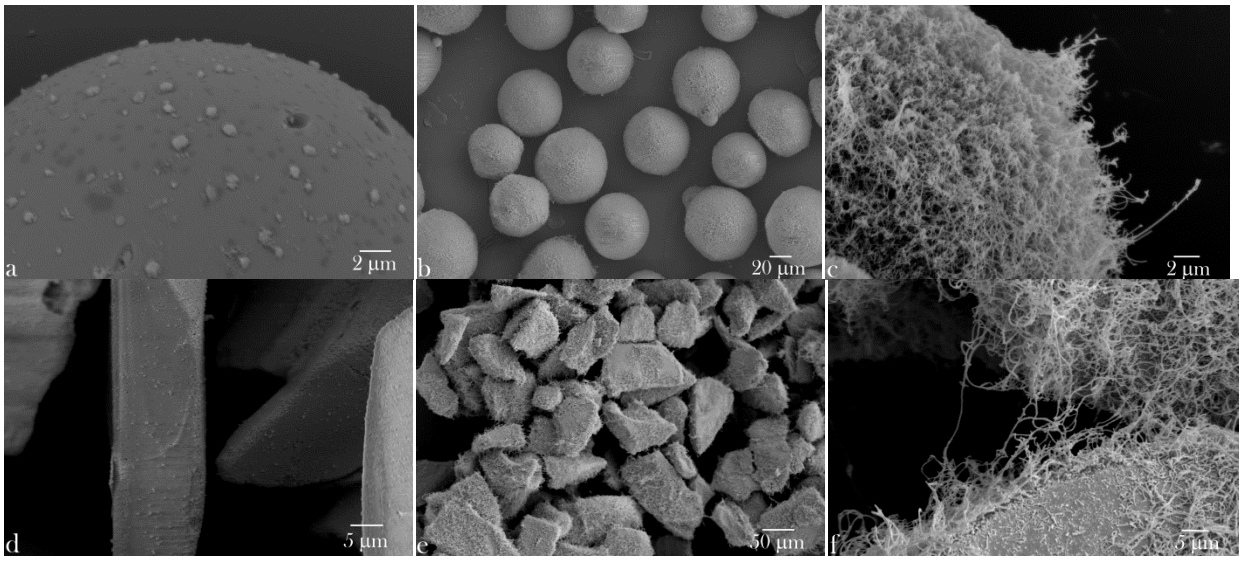

Figure 4.1. Scanning electron micrographs of spherical microparticles, (a) bare (S_B) and (b, c) coated with nanowires (S_{NW}), and irregularly planar microparticles, (d) bare (P_B) and (e, f) coated with nanowires (P_{NW}), imaged under different magnifications.

Since a major goal of drug delivery is to maintain the drug levels within the therapeutic window with a minimal dosage, the drug loading capacity is a primary criterion determining the therapeutic effectiveness of a device. Therefore, we tested different shapes of microparticles, P_{NW} and S_{NW}, for their ability to capture insulin and elute it in 4 hours, which is a rough retention time of microparticles in small intestine.

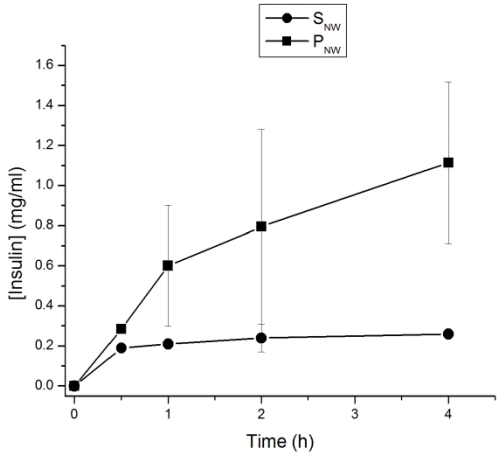

Figure 4.2. Temporal concentration profile for the elution of insulin from different microparticles.

Fig. 4.2 shows the drug elution profile of insulin-loaded microparticles, S_{NW} and P_{NW}. Spherical particles displayed no significant concentration changes as a function of elution time, while P_{NW} ones demonstrated a continuous increase of eluted insulin concentration in direct proportion to the incubation time, approaching a constant release rate for 1 – 4 h time period. P_{NW} demonstrated approximately 5 times higher insulin loading capacity than S_{NW}. Geometric

calculations based on the results of the morphological analysis of S and P particles (Fig.1) showed that the surface area of P particles is 3 – 3.5 times higher than that of S ones in the samples of identical weight, explaining why the loading efficiency was higher for P_{NW} particles than for S_{NW} ones. As expected, P_{NW} particles adsorbed more insulin than P_B due to (a) the additional surface area created by nanowires, and (b) the capillary effect by which they are able to effectively capture drug molecules in spite of the unfavorable concentration gradients.

One of the biggest challenges faced by oral drug delivery devices is the delivery of drugs across the epithelium without compromising the selective permeability of the latter. The permeability tests were conducted in order to measure the amount of insulin delivered across Caco-2 cell monolayers. As shown in Fig. 4.3, all spherical particles induced lower levels of permeability in comparison to P_{NW}, irrespective of whether the drug was loaded onto the particles prior to the test (Fig. 4.3a) or added separately to the apical compartments (Fig. 4.3b). P_{NW} has led to the highest concentration of basolateral insulin and, when particles loaded with insulin were applied, a drug delivery profile typified by a gradually increasing cumulative concentration of the released drug for the first 2 h of incubation was obtained.

4.3.2 Particle treatment to CaCO2 cells

Drug permeation across the epithelium is in this case expected to be driven by two factors: (a) drug elution and (b) particle geometry. Lying flat on the cell monolayer surface, a P_{NW} particle with its large surface can be visualized to impede the bulk diffusion of the drug across the underlying epithelium, an effect that could be circumvented by releasing the drug directly off the particle surface in contact with the epithelium.

The shape of microparticles influences the permeability of insulin across Caco-2 cell monolayers. Both the surface area in contact with the epithelium and the actual nanotopography are presumed to affect the mechanotransduction pathways that allow for an effective transepithelial transport of the drug. Increased permeability of small molecules across the epithelium induced by S_{NW} particles was reported previously[56]. For P particles, the surface nanowires induced a twofold increase in permeability versus nanowire-free particles, an effect that is more pronounced than the previously reported one. The augmented effect of P_{NW} particles in comparison with S_{NW} can be explained by the larger surface area of interaction between the nanowires and the epithelium.

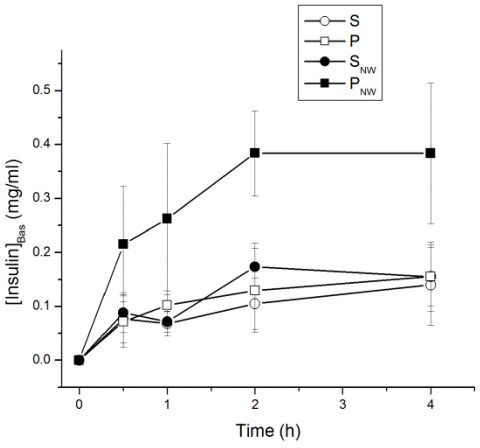

a)

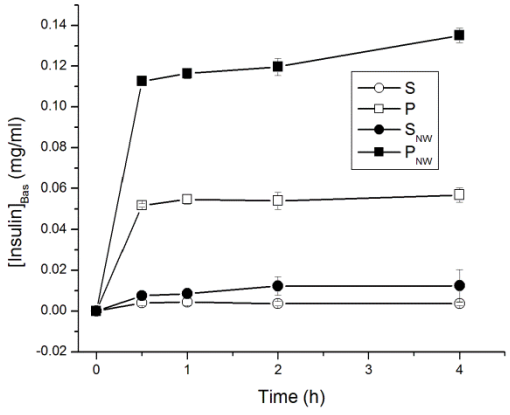

b)

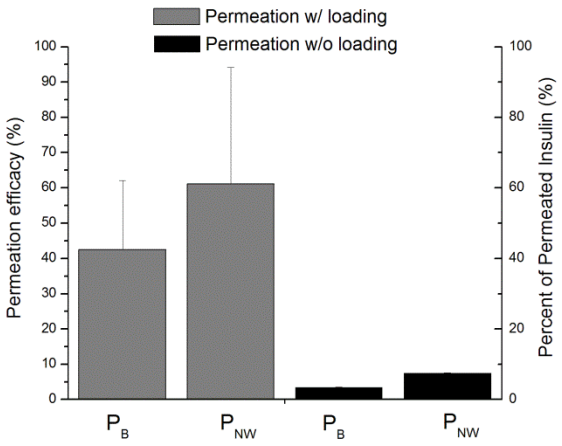

c)

Figure 4.3. (a) Concentration of insulin permeated across the Caco-2 cell layer membrane upon the application of different particles loaded with insulin: S_B, S_{NW}, P_B, and P_{NW}; (b) concentration of insulin permeated across the Caco-2 cell layer membrane when the particles and insulin were added separately to the apical compartments; (c) permeation efficacy using insulin-loaded P_{NW} particles and the percentage of permeated insulin when P_{NW} particles and insulin were added separately, after 30 min incubation. Permeation efficacy was calculated as a ratio between the eluted amount of the drug and the permated amount of the drug.

To examine the effects of P_{NW} particles on the integrity of the tight junction, an intercellular protein complex that regulates the paracellular transport of molecules across the epithelium[60,61], a morphological comparison between cell monolayers treated with S_{NW} and P_{NW} was conducted after the 4 h delivery. As shown in Fig.4.4a-b, P_{NW} particles showed a clear tendency to ruffle the ZO-1 pattern, indicating a mildly disruptive effect on the tight junction, through which a higher rate of drug delivery across the epithelium is enabled. Approximately 60 - 70 % of the ZO-1 pattern lined up along the tight junction was ruffled upon the application of 5 mg of NW particles per cm^2, as opposed to only 8 % in the control sample and 10 % in the sample incubated with an equal amount of S_{NW} microbeads. Such a jagged profile of a junctional protein, along with occasionally seen double lines, is an indicator of a structurally disrupted, but not dysfunctional epithelial membrane[62,63]. A comparison of the fluorescence intensity of the ZO-1 pattern normalized to the surface area yielded significantly lower intensity for ZO-1 of cells incubated with P_{NW} than for that incubated with S_{NW} or the negative control (Fig.4.4c). Since the paracellular permeability is thought to be inversely proportional to the density of tight junctional strands[64–66], the detected decrease in the density of the perijunctional ZO-1 molecules is directly indicative of an increased paracellular permeability of Caco-2 cell monolayers in contact with P_{NW} particles. Another observation consistent with the loosening of the tight junction that P_{NW} particles induced to a markedly greater extent than S_{NW} has come from the comparison of the width of the ZO-1 pattern. As also shown in Fig. 4.4c, in the presence of P_{NW} particles, it is twice lower with respect to both the negative control and the cells treated with S_{NW} particles. Once sufficient surface coverage of the cell monolayer by P_{NW} particles is achieved, any further addition of particles, mainly forming stacked-up agglomerates, does not contribute to a further decrease in the tight junction width (Fig. 4.4d). These results also confirm that TJ

loosening is more likely to be caused by nanostructures than by the weight effect of microparticles on the underlying epithelium.

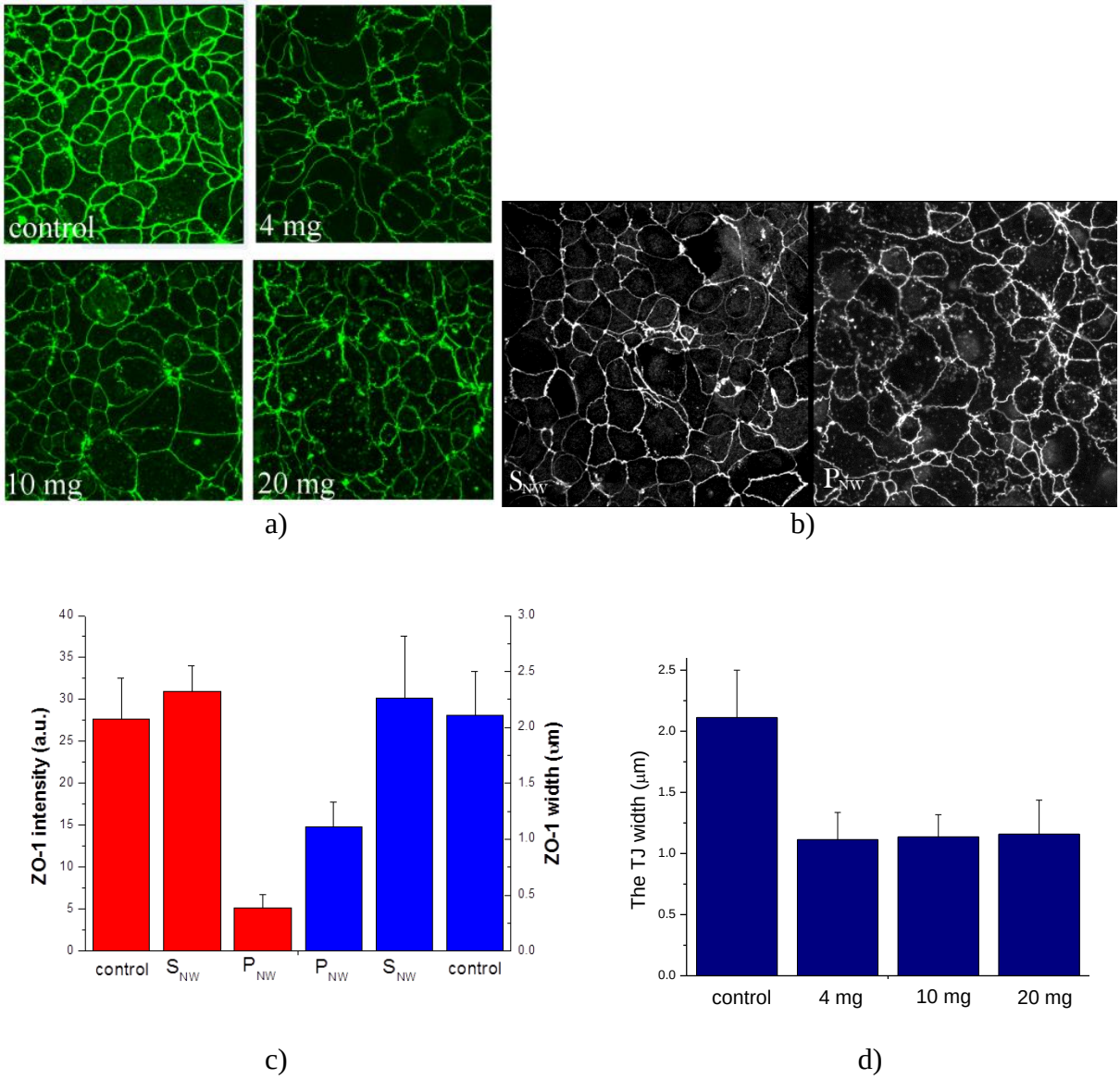

Figure 4.4. (a) Fluorescent staining of ZO-1 molecules in Caco-2 cell monolayers treated for 4 h with no particles (control) and with different amounts of P_{NW} particles per cm^2, imaged under identical excitations; (b) a comparison between the fluorescently stained ZO-1 pattern of Caco-2 cell monolayers treated for 4 h with P_{NW} and S_{NW} particles; (c) a comparison between the average pixel intensity of ZO-1-tagged fluorescent IgG and the width of ZO-1 conglomerates at the tight junction for Caco-2 cells incubated without any particles (control) and in the presence of S_{NW} and P_{NW} particles; (d) a comparison between the width of ZO-1 conglomerates at the tight junction for Caco-2 cells incubated without any particles (control) and in the presence of different amounts of P_{NW} particles cm^2. All images were taken at 100 x magnification in oil. The size of each image is 750 x 750 μm^2.

Chapter 5. Conclusion

The focus of my research lies at the intersection of delivery vehicle design and therapeutic effect studies with an aim to develop new protein therapeutics. It has been an inspiring experience to study drug delivery, protein therapeutics, and genome engineering fields, which required knowledge in biology, chemistry, and medicine. I was particularly interested in understanding the interactions between macromolecules and investigating the ways to utilize these interactions to engineer protein delivery systems. Efficient Cas9 protein loading was achieved with the interaction of Cas9 protein to DNA conjugated gold nanoparticle and sequence specific interaction of a transcription factor to DNA was an interesting starting point of novel delivery vehicle design. This dissertation research investigated how novel delivery systems are developed using a variety of molecular structures for delivery of protein therapeutic candidates.

We present a gold nanoparticle-based delivery vehicle, CRISPR-Gold, which can deliver Cas9 protein, guide RNA, and donor DNA *in vivo*. The big challenge to load all three macromolecules in a single particle was achieved with a DNA conjugated gold nanoparticle core. CRISPR-Gold proved its efficiency in various primary cells and human stem cells by homology directed repair DNA editing. Moreover, CRISPR-Gold corrected a dystrophin gene mutation that causes Duchenne muscular dystrophy and restored dystrophin protein expression in mouse muscle after a single injection. CRISPR-Gold is the first example of a non-viral delivery vehicle that can induce HDR *in vivo* and has the potential to treat a wide array of genetic diseases. This work has the potential to have a significant impact on medicine, given the large number of genetic diseases that can be treated with Cas9-mediated genome editing.

Another delivery vehicle was inspired by the interaction between protein and DNA. DARTs were designed to deliver transcription factors using a multifunctional oligonucleotide, which has multiple advantages including a small size and efficient delivery without chemically modifying proteins. DARTs delivered transcription factor Nrf2 in mice with acetaminophen induced liver injuries. The DART delivery strategy has numerous potential applications given the central role of transcription factors in liver biology. In addition, it should be possible to deliver transcription factors to cell types outside of the liver by using targeting groups other than galactose. Importantly, the DART delivery strategy demonstrates that DNA based scaffolds can be used to deliver DNA binding proteins and provides a platform for the development of DNA origami-based delivery vehicles.

An adjacent focus of protein delivery research expands the field of oral drug delivery. We studied the shape effect of nanostructured microparticles to engineer this particle system to overcome the challenges of protein oral delivery. Shape and texture of the particles were optimized to promote adhesion by means of simple steric effects. In this work, we have shown that irregularly planar silica particles coated with silicon nanowires exhibited a higher drug loading capacity than their spherical counterparts owing to their three times larger surface area per unit weight. Simultaneously, as a result of a larger surface area in contact with the cell layer, the planar particles increased the transepithelial permeation of a moderately sized model drug, insulin. This research opened the doors to the creative use of geometry in future devices aiming to incorporate this technology for various biomedical applications.

References

(1) Doudna, J. A.; Charpentier, E. The New Frontier of Genome Engineering with CRISPR-Cas9. *Science (80-.).* **2014**, *346*, 1258096–1258096.

(2) Jinek, M.; Chylinski, K.; Fonfara, I.; Hauer, M.; Doudna, J. A.; Charpentier, E. A Programmable Dual-RNA – Guided DNA Endonuclease in Adaptive Bacterial Immunity. *Science (80-.).* **2012**, *337*, 816–822.

(3) Cong, L.; Ran, F. A.; Cox, D.; Lin, S.; Barretto, R.; Habib, N.; Hsu, P. D.; Wu, X.; Jiang, W.; Marraffini, L. A.; *et al.* Multiplex Genome Engineering Using CRISPR/Cas Systems. *Science* **2013**, *339*, 819–823.

(4) Cho, S. W.; Kim, S.; Kim, J. M.; Kim, J.-S. Targeted Genome Engineering in Human Cells with the Cas9 RNA-Guided Endonuclease. *Nat. Biotechnol.* **2013**, *31*, 230–232.

(5) Kim, S.; Kim, D.; Cho, S. W.; Kim, J.; Kim, J. S. Highly Efficient RNA-Guided Genome Editing in Human Cells via Delivery of Purified Cas9 Ribonucleoproteins. *Genome Res.* **2014**, *24*, 1012–1019.

(6) Cong, L.; Ran, F. A.; Cox, D.; Lin, S.; Barretto, R.; Habib, N.; Hsu, P. D.; Wu, X.; Jiang, W.; Marraffini, L. A.; *et al.* Multiplex Genome Engineering Using CRISPR/Cas System. *Science (80-.).* **2013**, 819–823.

(7) Lin, S.; Staahl, B.; Alla, R. K.; Doudna, J. a. Enhanced Homology-Directed Human Genome Engineering by Controlled Timing of CRISPR/Cas9 Delivery. *Elife* **2014**, *3*, 1–13.

(8) Schumann, K.; Lin, S.; Boyer, E.; Simeonov, D. R.; Subramaniam, M.; Gate, R. E.; Haliburton, G. E.; Ye, C. J.; Bluestone, J. a.; Doudna, J. a.; *et al.* Generation of Knock-in Primary Human T Cells Using Cas9 Ribonucleoproteins. *Proc. Natl. Acad. Sci. U. S. A.* **2015**, *112*, 201512503.

(9) Sander, J. D.; Joung, J. K. CRISPR-Cas Systems for Editing, Regulating and Targeting Genomes. *Nat. Biotechnol.* **2014**, *32*, 347–355.

(10) Xu, L.; Park, K. H.; Zhao, L.; Xu, J.; El Refaey, M.; Gao, Y.; Zhu, H.; Ma, J.; Han, R. CRISPR-Mediated Genome Editing Restores Dystrophin Expression and Function in Mdx Mice. *Mol. Ther.* **2015**.

(11) Ran, F. A.; Cong, L.; Yan, W. X.; Scott, D. a.; Gootenberg, J. S.; Kriz, A. J.; Zetsche, B.; Shalem, O.; Wu, X.; Makarova, K. S.; *et al.* In Vivo Genome Editing Using Staphylococcus Aureus Cas9. *Nature* **2015**, *520*, 186–190.

(12) Ousterout, D. G.; Kabadi, A. M.; Thakore, P. I.; Majoros, W. H.; Reddy, T. E.; Gersbach, C. a. Multiplex CRISPR/Cas9-Based Genome Editing for Correction of Dystrophin Mutations That Cause Duchenne Muscular Dystrophy. *Nat. Commun.* **2015**, *6*, 6244.

(13) Long, C.; McAnally, J. R.; Shelton, J. M.; Mireault, A. A.; Bassel-Duby, R.; Olson, E. N. Prevention of Muscular Dystrophy in Mice by CRISPR/Cas9-Mediated Editing of Germline DNA. *Science* **2014**, *345*, 1184–1188.

(14) Long, C.; McAnally, J. R.; Shelton, J. M.; Mireault, A. A.; Bassel-Duby, R.; Olson, E. N. Prevention of Muscular Dystrophy in Mice by CRISPR/Cas9-Mediated Editing of Germline DNA. *Science (80-.).* **2014**, *345*, 1184–1188.

(15) Stedman, H. H.; Sweeney, H. L.; Shrager, J. B.; Maguire, H. C.; Panettieri, R. A.; Petrof, B.; Narusawa, M.; Leferovich, J. M.; Sladky, J. T.; Kelly, A. M. The Mdx Mouse Diaphragm Reproduces the Degenerative Changes of Duchenne Muscular Dystrophy. *Nature* **1991**, *352*, 536–539.

(16) Ding, Y.; Jiang, Z.; Saha, K.; Kim, C. S.; Kim, S. T.; Landis, R. F.; Rotello, V. M. Gold

Nanoparticles for Nucleic Acid Delivery. *Mol. Ther.* **2014**, *22*, 1075–1083.
(17) Ghosh, P. S.; Kim, C.-K.; Han, G.; Forbes, N. S.; Rotello, V. M. Efficient Gene Delivery Vectors by Tuning the Surface Charge Density of Amino Acid-Functionalized Gold Nanoparticles. *ACS Nano* **2008**, *2*, 2213–2218.
(18) Yang, L.; Guell, M.; Byrne, S.; Yang, J. L.; De Los Angeles, A.; Mali, P.; Aach, J.; Kim-Kiselak, C.; Briggs, A. W.; Rios, X.; *et al.* Optimization of Scarless Human Stem Cell Genome Editing. *Nucleic Acids Res.* **2013**, *41*, 9049–9061.
(19) Fu, Y.; Sander, J. D.; Reyon, D.; Cascio, V. M.; Joung, J. K. Improving CRISPR-Cas Nuclease Specificity Using Truncated Guide RNAs. *Nat. Biotechnol.* **2014**, *32*, 279–284.
(20) Conboy, M. J.; Conboy, I. M.; Rando, T. a. Heterochronic Parabiosis: Historical Perspective and Methodological Considerations for Studies of Aging and Longevity. *Aging Cell* **2013**, *12*, 525–530.
(21) Conboy, M. J.; Cerletti, M.; Wagers, A. J.; Conboy, I. M. Immuno-Analysis and FACS Sorting of Adult Muscle Fiber-Associated Stem/precursor Cells. *Methods Mol. Biol.* **2010**, *621*, 165–173.
(22) Pigozzo, S. R.; Da Re, L.; Romualdi, C.; Mazzara, P. G.; Galletta, E.; Fletcher, S.; Wilton, S. D.; Vitiello, L. Revertant Fibers in the Mdx Murine Model of Duchenne Muscular Dystrophy: An Age- and Muscle-Related Reappraisal. *PLoS One* **2013**, *8*, e72147.
(23) Takahashi, K.; Yamanaka, S. Induction of Pluripotent Stem Cells from Mouse Embryonic and Adult Fibroblast Cultures by Defined Factors. *Cell* **2006**, *126*, 663–676.
(24) Barkett, M.; Gilmore, T. D. Control of Apoptosis by Rel/NF-kappaB Transcription Factors. *Oncogene* **1999**, *18*, 6910–6924.
(25) Huang, P.; He, Z.; Ji, S.; Sun, H.; Xiang, D.; Liu, C.; Hu, Y.; Wang, X.; Hui, L. Induction of Functional Hepatocyte-like Cells from Mouse Fibroblasts by Defined Factors. *Nature* **2011**, *475*, 386–389.
(26) Giudice, A.; Arra, C.; Turco, M. C. Review of Molecular Mechanisms Involved in the Activation of the Nrf2-ARE Signaling Pathway by Chemopreventive Agents. *Methods Mol Biol* **2010**, *647*, 37–74.
(27) Bataille, a M.; Manautou, J. E. Nrf2: A Potential Target for New Therapeutics in Liver Disease. *Clin. Pharmacol. Ther.* **2012**, *92*, 340–348.
(28) Mitsuishi, Y.; Taguchi, K.; Kawatani, Y.; Shibata, T.; Nukiwa, T.; Aburatani, H.; Yamamoto, M.; Motohashi, H. Nrf2 Redirects Glucose and Glutamine into Anabolic Pathways in Metabolic Reprogramming. *Cancer Cell* **2012**, *22*, 66–79.
(29) Cuadrado, A.; Moreno-Murciano, P.; Pedraza-Chaverri, J. The Transcription Factor Nrf2 as a New Therapeutic Target in Parkinson's Disease. *Expert Opin. Ther. Targets* **2009**, *13*, 319–329.
(30) Crawford, R.; Erben, C. M.; Periz, J.; Hall, L. M.; Brown, T.; Turberfield, A. J.; Kapanidis, A. N. Non-Covalent Single Transcription Factor Encapsulation inside a DNA Cage. *Angew. Chemie - Int. Ed.* **2013**, *52*, 2284–2288.
(31) Liu, Y.; Wang, H.; Kamei, K.; Yan, M.; Chen, K.-J.; Yuan, Q.; Shi, L.; Lu, Y.; Tseng, H.-R. Delivery of Intact Transcription Factor by Using Self-Assembled Supramolecular Nanoparticles. *Angew. Chem. Int. Ed. Engl.* **2011**, *50*, 3058–3062.
(32) Yan, M.; Du, J.; Gu, Z.; Liang, M.; Hu, Y.; Zhang, W.; Priceman, S.; Wu, L.; Zhou, Z. H.; Liu, Z.; *et al.* A Novel Intracellular Protein Delivery Platform Based on Single-Protein Nanocapsules. *Nat. Nanotechnol.* **2010**, *5*, 48–53.
(33) Lorin, A.; Noël, M.; Provencher, M. È.; Turcotte, V.; Masson, C.; Cardinal, S.; Lagüe, P.;

Voyer, N.; Auger, M. Revisiting Peptide Amphiphilicity for Membrane Pore Formation. *Biochemistry* **2011**, *50*, 9409–9420.
(34) Lee, K.; Rafi, M.; Wang, X.; Aran, K.; Feng, X.; Lo Sterzo, C.; Tang, R.; Lingampalli, N.; Kim, H. J.; Murthy, N. In Vivo Delivery of Transcription Factors with Multifunctional Oligonucleotides. *Nat. Mater.* **2015**, *14*, 701–706.
(35) Murthy, N.; Campbell, J.; Fausto, N.; Hoffman, A. S.; Stayton, P. S. Bioinspired pH-Responsive Polymers for the Intracellular Delivery of Biomolecular Drugs. *Bioconjug. Chem.* **2003**, *14*, 412–419.
(36) Lee, K.; Lee, H.; Lee, K. W.; Park, T. G. Optical Imaging of Intracellular Reactive Oxygen Species for the Assessment of the Cytotoxicity of Nanoparticles. *Biomaterials* **2011**, *32*, 2556–2565.
(37) Dube, D.; Khatri, K.; Goyal, A. K.; Mishra, N.; Vyas, S. P. Preparation and Evaluation of Galactosylated Vesicular Carrier for Hepatic Targeting of Silibinin. *Drug Dev. Ind. Pharm.* **2010**, *36*, 547–555.
(38) Chan, K.; Han, X. D.; Kan, Y. W. An Important Function of Nrf2 in Combating Oxidative Stress: Detoxification of Acetaminophen. *Proc. Natl. Acad. Sci. U. S. A.* **2001**, *98*, 4611–4616.
(39) Larson, A. M.; Polson, J.; Fontana, R. J.; Davern, T. J.; Lalani, E.; Hynan, L. S.; Reisch, J. S.; Schi??dt, F. V.; Ostapowicz, G.; Shakil, A. O.; *et al.* Acetaminophen-Induced Acute Liver Failure: Results of a United States Multicenter, Prospective Study. *Hepatology* **2005**, *42*, 1364–1372.
(40) Tao, S. L.; Desai, T. A. Microfabricated Drug Delivery Systems: From Particles to Pores. *Advanced Drug Delivery Reviews*, 2003, *55*, 315–328.
(41) Thakar, R. G.; Chown, M. G.; Patel, A.; Peng, L.; Kumar, S.; Desai, T. A. Contractility-Dependent Modulation of Cell Proliferation and Adhesion by Microscale Topographical Cues. *Small* **2008**, *4*, 1416–1424.
(42) Motlagh, D.; Senyo, S. E.; Desai, T. A.; Russell, B. Microtextured Substrata Alter Gene Expression, Protein Localization and the Shape of Cardiac Myocytes. *Biomaterials* **2003**, *24*, 2463–2476.
(43) Ainslie, K. M.; Tao, S. L.; Popat, K. C.; Desai, T. A. In Vitro Immunogenicity of Silicon-Based Micro- and Nanostructured Surfaces. *ACS Nano* **2008**, *2*, 1076–1084.
(44) Decuzzi, P.; Pasqualini, R.; Arap, W.; Ferrari, M. Intravascular Delivery of Particulate Systems: Does Geometry Really Matter? *Pharmaceutical Research*, 2009, *26*, 235–243.
(45) Lee, S. Y.; Ferrari, M.; Decuzzi, P. Design of Bio-Mimetic Particles with Enhanced Vascular Interaction. *J. Biomech.* **2009**, *42*, 1885–1890.
(46) Van De Ven, A. L.; Kim, P.; Haley, O.; Fakhoury, J. R.; Adriani, G.; Schmulen, J.; Moloney, P.; Hussain, F.; Ferrari, M.; Liu, X.; *et al.* Rapid Tumoritropic Accumulation of Systemically Injected Plateloid Particles and Their Biodistribution. *J. Control. Release* **2012**, *158*, 148–155.
(47) Uskoković, V. Insights into Morphological Nature of Precipitation of Cholesterol. *Steroids* **2008**, *73*, 356–369.
(48) Uskoković, V. Composites Comprising Cholesterol and Carboxymethyl Cellulose. *Colloids Surfaces B Biointerfaces* **2008**, *61*, 250–261.
(49) Fasinu, P.; Pillay, V.; Ndesendo, V. M. K.; Du Toit, L. C.; Choonara, Y. E. Diverse Approaches for the Enhancement of Oral Drug Bioavailability. *Biopharm. Drug Dispos.* **2011**, *32*, 185–209.

(50) Soares, A. F.; Carvalho, R. D. A.; Veiga, F. Oral Administration of Peptides and Proteins: Nanoparticles and Cyclodextrins as Biocompatible Delivery Systems. *Nanomedicine (Lond).* **2007**, *2*, 183–202.
(51) Basit, A. W. Advances in Colonic Drug Delivery. *Drugs*, 2005, *65*, 1991–2007.
(52) Tsaioun, K.; Kates, S. A. *ADMET for Medicinal Chemists: A Practical Guide*; 2010.
(53) Fischer, K. E.; Jayagopal, A.; Nagaraj, G.; Daniels, R. H.; Li, E. M.; Silvestrini, M. T.; Desai, T. a. Nanoengineered Surfaces Enhance Drug Loading and Adhesion. *Nano Lett.* **2011**, *11*, 1076–1081.
(54) Fischer, K. E.; Nagaraj, G.; Hugh Daniels, R.; Li, E.; Cowles, V. E.; Miller, J. L.; Bunger, M. D.; Desai, T. a. Hierarchical Nanoengineered Surfaces for Enhanced Cytoadhesion and Drug Delivery. *Biomaterials* **2011**, *32*, 3499–3506.
(55) Fischer, K. E.; Alemán, B. J.; Tao, S. L.; Daniels, R. H.; Li, E. M.; Bünger, M. D.; Nagaraj, G.; Singh, P.; Zettl, A.; Desai, T. A. Biomimetic Nanowire Coatings for next Generation Adhesive Drug Delivery Systems. *Nano Lett.* **2009**, *9*, 716–720.
(56) Uskoković, V.; Lee, P. P.; Walsh, L. a.; Fischer, K. E.; Desai, T. a. PEGylated Silicon Nanowire Coated Silica Microparticles for Drug Delivery across Intestinal Epithelium. *Biomaterials* **2012**, *33*, 1663–1672.
(57) Artursson, P.; Karlsson, J. Correlation between Oral Drug Absorption in Humans and Apparent Drug Permeability Coefficients in Human Intestinal Epithelial (Caco-2) Cells. *Biochem. Biophys. Res. Commun.* **1991**, *175*, 880–885.
(58) Yasumatsu, H.; Tanabe, S. The Casein Peptide Asn-Pro-Trp-Asp-Gln Enforces the Intestinal Tight Junction Partly by Increasing Occludin Expression in Caco-2 Cells. *Br. J. Nutr.* **2010**, *104*, 951–956.
(59) Alhamoruni, a; Lee, a C.; Wright, K. L.; Larvin, M.; O'Sullivan, S. E. Pharmacological Effects of Cannabinoids on the Caco-2 Cell Culture Model of Intestinal Permeability. *J. Pharmacol. Exp. Ther.* **2010**, *335*, 92–102.
(60) Yeh, T. H.; Hsu, L. W.; Tseng, M. T.; Lee, P. L.; Sonjae, K.; Ho, Y. C.; Sung, H. W. Mechanism and Consequence of Chitosan-Mediated Reversible Epithelial Tight Junction Opening. *Biomaterials* **2011**, *32*, 6164–6173.
(61) Johnson, P. H.; Frank, D.; Costantino, H. R. Discovery of Tight Junction Modulators: Significance for Drug Development and Delivery. *Drug Discovery Today*, 2008, *13*, 261–267.
(62) Moyes, S. M.; Morris, J. F.; Carr, K. E. Macrophages Increase Microparticle Uptake by Enterocyte-like Caco-2 Cell Monolayers. *J. Anat.* **2010**, *217*, 740–754.
(63) Liu, M.; Yang, X.; Fan, J.; Zhang, R.; Wu, J.; Zeng, Y.; Nie, J.; Yu, X. Altered Tight Junctions and Fence Function in NRK-52E Cells Induced by Aristolochic Acid. *Hum. Exp. Toxicol.* **2012**, *31*, 32–41.
(64) Claude, P. Morphological Factors Influencing Transepithelial Permeability: A Model for the Resistance of the Zonula Occludens. *J. Membr. Biol.* **1978**, *39*, 219–232.
(65) Marcial, M. A.; Carlson, S. L.; Madara, J. L. Partitioning of Paracellular Conductance along the Ileal Crypt-Villus Axis: A Hypothesis Based on Structural Analysis with Detailed Consideration of Tight Junction Structure-Function Relationships. *J. Membr. Biol.* **1984**, *80*, 59–70.
(66) Shen, L.; Weber, C. R.; Raleigh, D. R.; Yu, D.; Turner, J. R. Tight Junction Pore and Leak Pathways: A Dynamic Duo. *Annu. Rev. Physiol.* **2011**, *73*, 283–309.